Progress in Oceanography 210 (2023) 102925

Contents lists available at ScienceDirect

Progress in Oceanography

journal homepage: www.elsevier.com/locate/pocean

The Brazil Current quasi-stationary unstable meanders at 22°S–23°S

Ilson C.A. da Silveira [a,1], Filipe Pereira [a,b,*,1], Glenn R. Flierl [c], Iury T. Simoes-Sousa [d], André Palóczy [e], Milton Borges-Silva [a], César B. Rocha [f]

[a] Instituto Oceanográfico, Universidade de São Paulo, São Paulo, SP, Brazil
[b] School for Marine Science & Technology, University of Massachusetts Dartmouth, New Bedford, MA, United States
[c] Department of Earth, Atmospheric and Planetary Sciences, Massachusetts Institute of Technology, Cambridge, MA, United States
[d] Mechanical Engineering Department, University of Massachusetts Dartmouth, Dartmouth, MA, United States
[e] Department of Geosciences, University of Oslo, Oslo, Norway
[f] Department of Marine Sciences, University of Connecticut, Groton, CT, United States

ARTICLE INFO

Dataset link: https://www. marinha.mil.br/chm/dados-do-bndo/outros-dados-e-produtos, https://podaac.jpl.nasa.gov, https://aviso.altimetry.fr, 10.24400/527896/a01-2021.001, 10.24400/527896/a01-2021.002, https://marine.copernicus.eu/, 10.5285/c6612cbe-50b3-0cff-e053-6c86abc09f8f, https://www.gebco.net/

Keywords:
Brazil current
Baroclinic instability
Mesoscale eddies
Western boundary currents
Conservation of potential vorticity
Contour dynamics
South Atlantic
Cape Frio
Cape São Tomé

ABSTRACT

The most conspicuous oceanographic features off Southeast Brazil are the quasi-stationary eddies formed off Capes São Tomé (CSTE) and Frio (CFE) associated with the Brazil Current (BC). We use SST and SSH products to infer eddy growth rates. These two independent data sets reveal an average growth rate of 0.06 day^{-1}, and propagation speeds are virtually null. CFE tends to be more unstable and frequent than CSTE (3.5 vs. 2.3 events per year). CSTE can propagate toward the north or south while CFE only propagates southward. We perform potential vorticity (PV) inversion calculation using hydrographic data to understand how the meander growth occurs in the baroclinic jet formed by the BC and the Intermediate Western Boundary Current (IWBC). PV anomalies in one layer enhanced the anomalies on the other. This result offered *in situ* evidence of baroclinic conversion occurring during the eddy event captured in the observations. We then build a theoretical two-layer model calibrated with the observations seeking to explain why the eddies grow in place, and no accompanying unstable anticyclones are formed. The experiments lead us to conclude that the eddies' quasi-stationarity is due to the almost pure baroclinic nature of the BC-IWBC jet. We also find that the western boundary inhibits the formation of the anticyclones. As observed in satellite imagery, the meanders develop as isolated disturbances that may grow simultaneously or not.

1. Introduction

The Brazil Current (BC) is the western boundary current that flows along the Southeastern Brazilian continental margin (20°S–26°S), closing the South Atlantic Subtropical Gyre. Its core is typically centered at the 800–1400 m isobath range, with velocities exceeding 0.5 m s^{-1} and occupying the upper 500 m (Silveira et al., 2000b, 2004). With a volume transport ranging from 1 to 7 Sv (Schmid and Majumder, 2018) off Southeast (SE) Brazil, the BC carries two water masses poleward: the warm and salty Tropical Water (TW) at surface levels, and the relative colder and fresher South Atlantic Central Water (SACW) at pycnocline levels (Stramma and England, 1999).

Underneath the BC, an undercurrent flows opposite, occupying 1000 m of the water column. This Intermediate Western Boundary Current (IWBC) has core velocities exceeding 0.25 m s^{-1} (Böebel et al., 1999; Silveira et al., 2004, 2008; Legeais et al., 2013; Biló et al., 2014). The IWBC transports northward about 6 Sv of Antarctic Intermediate Water (AAIW) and Upper Circumpolar Deep Water (UCDW) equatorward (Böebel et al., 1999; Silveira et al., 2004). The IWBC core is centered at 700–900 m and coincides with the salinity minimum associated with the AAIW (Silveira et al., 2004, 2008).

These opposite flowing currents form a largely first-mode baroclinic jet (the BC-IWBC jet), extending vertically from the surface down to intermediate depths (Silveira et al., 2008; Rocha et al., 2014; Biló et al., 2014) (Fig. 1). This vertical structure arises in part due to the São Paulo Plateau (22°S–28°S), a topographic feature that replaces the continental rise off Southeast Brazil and drastically reduces the steepness of the continental slope at depths greater than 2000 m (Souza and Sgarbi, 2019). The São Paulo Plateau moves offshore the Deep

* Corresponding author at: Instituto Oceanográfico, Universidade de São Paulo, São Paulo, SP, Brazil.
E-mail address: pereiraf@usp.br (F. Pereira).
[1] **Contributed equally to this work and share the first authorship.**

https://doi.org/10.1016/j.pocean.2022.102925
Received 6 May 2022; Received in revised form 30 September 2022; Accepted 22 November 2022
Available online 5 December 2022

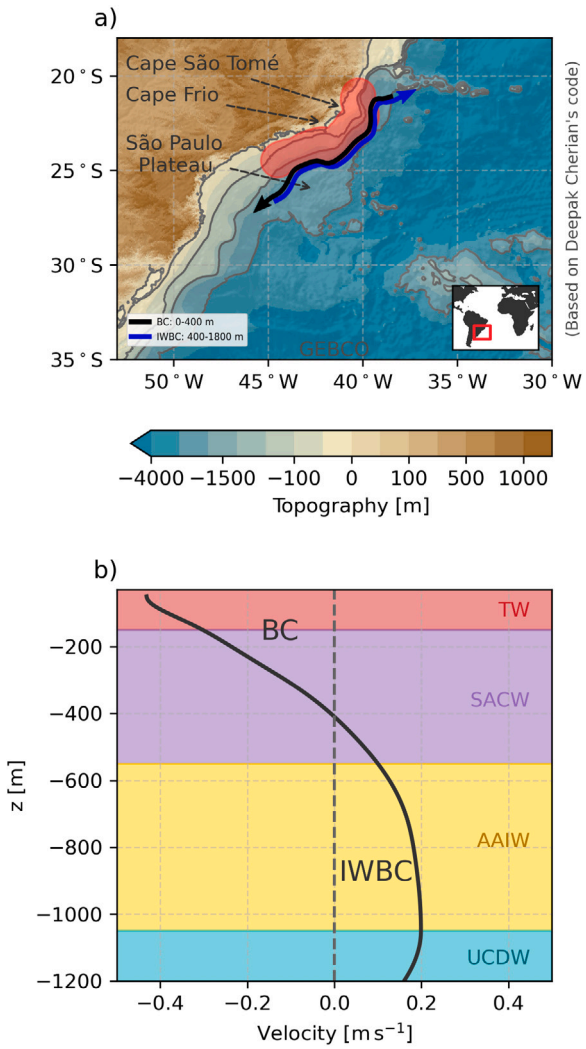

Fig. 1. (a) Topographic map of Southeast Brazil. The region highlighted in red depicts the area where the typical vertical structure of water masses and along-stream velocity of the Western Boundary Current System off Southeast Brazil occurs. The black and blue lines represent the Brazil Current (BC) and the Intermediate Western Boundary Current (IWBC) pathways, respectively. The color scale represents bottom topography obtained from GEBCO 2021. (b) BC occupies the upper 400 m of the water column, while the region between 500 m and 1800 m is the domain of the IWBC. The 25.7, 26.9 and 27.4 kg m^{-3} isopycnals indicate the climatological interfaces for Tropical Water (TW), South Atlantic Central Water (SACW), Antarctic Intermediate Water (AAIW), Upper Circumpolar Deep Water (UCDW), respectively.
Source: Adapted from Rocha et al. (2014).

Western Boundary Current (DWBC), which transports North Atlantic Deep Water (NADW) southward, thereby leading to a single velocity inversion on the continental slope.

Silveira et al. (2008) investigated the BC-IWBC jet based on current meter mooring data off Southeast Brazil (see also Rocha et al., 2014), showing that the mean vertical structure of the along-isobath currents is largely accounted for by the first baroclinic mode. Silveira et al. (2008) found that the jet is 98% baroclinic with the first mode alone accounting for 84% of the variability of the vertical structure.

Conspicuous cyclonic meanders associated with the BC-IWBC jet frequently develop off Cape São Tomé (CST, 22°S) and Cape Frio (CF, 23°S). These meanders were first described by Mascarenhas Jr. et al. (1971) from synoptic hydrographic data. The cyclones grow in amplitude and have little to no alongshore propagation (Garfield, 1990). Silveira et al. (2008) associated the meanders with troughs of unstable vorticity waves with wavelengths of 200–300 km. In addition, Mill et al. (2015) described CST eddies that neck off as isolated rings and translate either southward or northward. Combining current meter mooring analysis and linear stability calculations in a one-dimensional quasi-geostrophic (QG) model, Silveira et al. (2008) and Rocha et al. (2014) inferred baroclinic instability to be the primary mechanism driving the meanders' growth finding the steering level to be within the IWBC portion of the water column. They also found phase speeds to be negligible or very weak northward. Rocha et al. (2014) made further calculations by computing baroclinic conversions directly from the mooring time series, detecting positive (current-to-eddy) energy conversion in the whole water column with maximum values near the steering level between the BC and the IWBC.

Much of the phenomenology of these quasi-stationary meanders is not yet well understood, specifically:

1. The non-propagating character of the meanders was first reported by Garfield (1990). However, no information on their growth rates and phase speeds based on either *in situ* or satellite observations are available to date. Consequently, no quantitative assessment of the linear stability predictions made by Silveira et al. (2008) and Rocha et al. (2014) has been possible;
2. It is known that the leading-order mechanism that drives meander growth is baroclinic instability. Nevertheless, this knowledge derives from theoretical linear instability models (Silveira et al., 2008; Rocha et al., 2014) or full numerical simulations (Calado et al., 2008; Mano et al., 2009). No direct evidence of baroclinic growth has been described from *in situ* observations;
3. There is no explanation as to why the meanders tend to grow quasi-stationary. In addition, only speculations on why cyclone development is favored over anticyclone development are available in the literature (Calado et al., 2008).

In this study, we address these three issues. We seek to: 1. obtain observational estimates for growth rates in the BC-IWBC meanders; 2. search for baroclinic growth in *in situ* quasi-synoptic[2] cruise observations; 3. explore the dynamics of the BC-IWBC jet to answer why the meanders are quasi-stationary and why most cyclones are formed off the Southeastern Brazilian capes, hereafter referred to as the Two-cape Region.

The article is organized as follows: in Section 2, we present an analysis of satellite Sea Surface Temperature (SST) and sea level to estimate the linear stability properties of the meanders; in Section 3, we formulate and apply the two-layer approximation to the geostrophic velocity fields, computed from Conductivity–Temperature–Depth (CTD) profiler measurements; in Section 4, we employ a semi-analytical QG model to address the baroclinic instability phenomenon on an idealized BC-IWBC jet. With model parameters inspired by *in situ* observations, we use this model to investigate the nature of the quasi-stationary meander growth; finally, Section 5 summarizes our findings and presents our conclusions.

2. Satellite-derived evidence of meander growth

In this section, we present analyses using two satellite data sets: SST and sea surface height (SSH). The goal is to provide estimates of the linear stability properties derived from observations.

2.1. Sea surface temperature analysis

The SST data used is obtained from the Multi-sensor Ultra-high Resolution (MUR) SST analysis (Chin et al., 2017). This is a daily, 1 km-resolution product from the Physical Oceanography Distributed Active Archive Centre (PODAAC) system. MUR SST is a blended SST analysis

[2] The word "synoptic" refers to observations taken nearly at a single time relative to the timescale of interest and is interpreted as a "snapshot" of spatial information (Talley et al., 2011, Chapter 6.1).

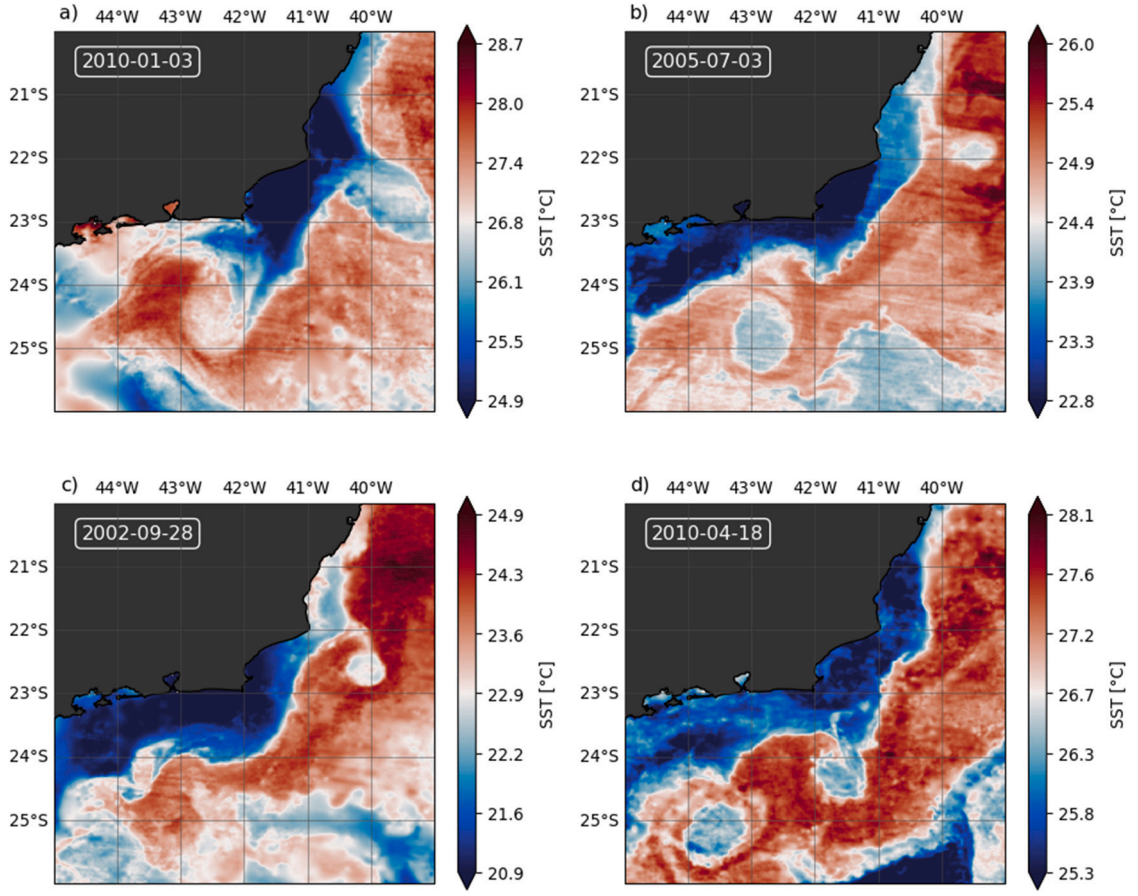

Fig. 2. Selected snapshots depict cyclonic meanders' formation off Capes São Tomé (22°S) and Frio (23°S). The color palette is Sea Surface Temperature (SST). The color scale varies between panels and is meant to enhance the visibility of the oceanic features in each image, i.e., white marks the mean SST value of each field.

that ingests data from both infrared (high resolution) and microwave (cloud-penetrating) instruments. An objective interpolation technique based on wavelet decomposition (Chin et al., 1998) is then used to blend these input data into gap-free fields, accounting for their different resolutions. Among other applications, the MUR SST data has been successfully used to quantitatively investigate phenomena associated with mesoscale SST fronts (*e.g.,* Vazquez-Cuervo et al., 2013).

We identify mature quasi-stationary meander events by inspecting SST images from 2002 to 2021 in the Two-cape Region. Here, mature events are interpreted as those which persisted and remained detectable for more than ten days. On average, $1.0 \pm 0.8\,\text{year}^{-1}$ mature events were detected in the 2002–2021 period. Nevertheless, cloud cover severely limited the number of useful images, despite the nominal gap-free 1 km resolution of the interpolated MUR SST product.

The SST front, interpreted here as the inshore edge of the BC jet (Silveira et al., 2008; Lorenzzetti et al., 2009), cannot be accurately resolved in all of the daily SST images, and the result of approximately $1\,\text{year}^{-1}$ should be thought of as a lower bound for the actual event frequency within the investigated time period.

Examples in which cyclonic meanders at CF and CST develop and are shed as cold-core rings nearly simultaneously are shown in Fig. 2a, b, respectively. This simultaneous meander growth was not the only mode of variability observed. Fig. 2c, d show events where meanders are seen to grow only at CST or at CF, respectively. There does not seem to be a preferred location for meanders to develop. Rather, it seems that unstable waves may be triggered at either cape. Fig. 2d shows a wave-like feature with wavelength of ~220 km, a representative value for the observed events in the SST data set.

We estimate the meander growth from the daily series of SST images by an edge-detection algorithm in each image, following the Otsu method (Othman et al., 2012) as proposed by Ramanantsoa et al. (2018). We select the meander troughs as the southernmost local minimum of the fronts using a reference point for each cape on the 180 m isobath (roughly the position of the mean SST front). We then use the meander troughs to estimate the growth rates via a linear least-squares approximation to an exponential fitting, as the example shown in Fig. 3. Similarly, mean phase speeds are estimated based on the displacement of the SST front perturbations between the first and the last day of each event and define a downstream propagation as negative.

The growth rates (phase speeds) for the CST events range from $0.07\,\text{day}^{-1}$ to $0.2\,\text{day}^{-1}$ ($-0.2\,\text{m s}^{-1}$ to $+0.05\,\text{m s}^{-1}$). Off CF, the estimated growth rates (phase speeds) are similar. They range from $0.06\,\text{day}^{-1}$ to $0.3\,\text{day}^{-1}$ ($-0.1\,\text{m s}^{-1}$ to $+0.01\,\text{m s}^{-1}$). The reader will find the results obtained for the exponential growth rates (σ) and phase speeds (c) from 2003 to 2021 in Appendix A.

2.2. Sea surface height analysis

We next explore a value-added altimetry product in addition to the SST-derived estimates for the meanders' growth rates. The Mesoscale Eddy Trajectories Atlas multi-satellite delayed-time product (META3.1-exp) was produced by SSALTO/DUACS and distributed by AVISO+ with support from CNES, in collaboration with IMEDEA (Pegliasco et al., 2021). The META3.1exp employs an eddy-detection method derived from the py-eddy-tracker algorithm (Mason et al., 2014) applied to 27 years of altimetry data (1993–2020) from the global gridded level 4 merged product (Taburet et al., 2019). The tracking algorithm relies on overlapping SSH contours and includes virtual observations to filter short trajectories. Furthermore, the product uses absolute dynamic

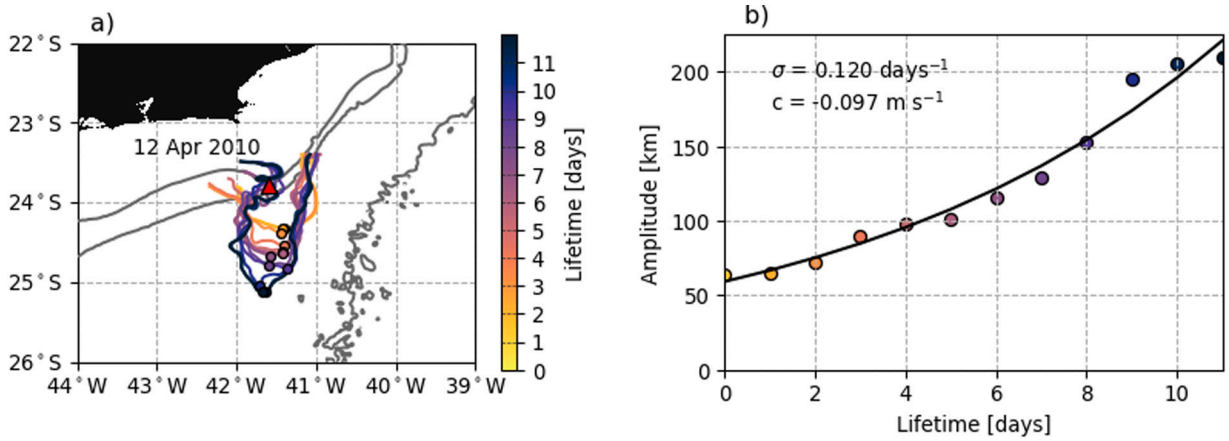

Fig. 3. Example of the exponential fitting used to estimate growth rates (σ) of meander growth events identified in the sea surface temperature analysis. (a) The fronts used in the fit starting on 12 April 2010. Dots mark the meander trough amplitudes, the red triangle marks the reference point on the 180 m for Cape Frio events, and the gray contours correspond to the 180 m, 1000 m and 3000 m isobaths. (b) Exponential fitting to the meander amplitudes with the estimated σ and the mean phase speed (c).

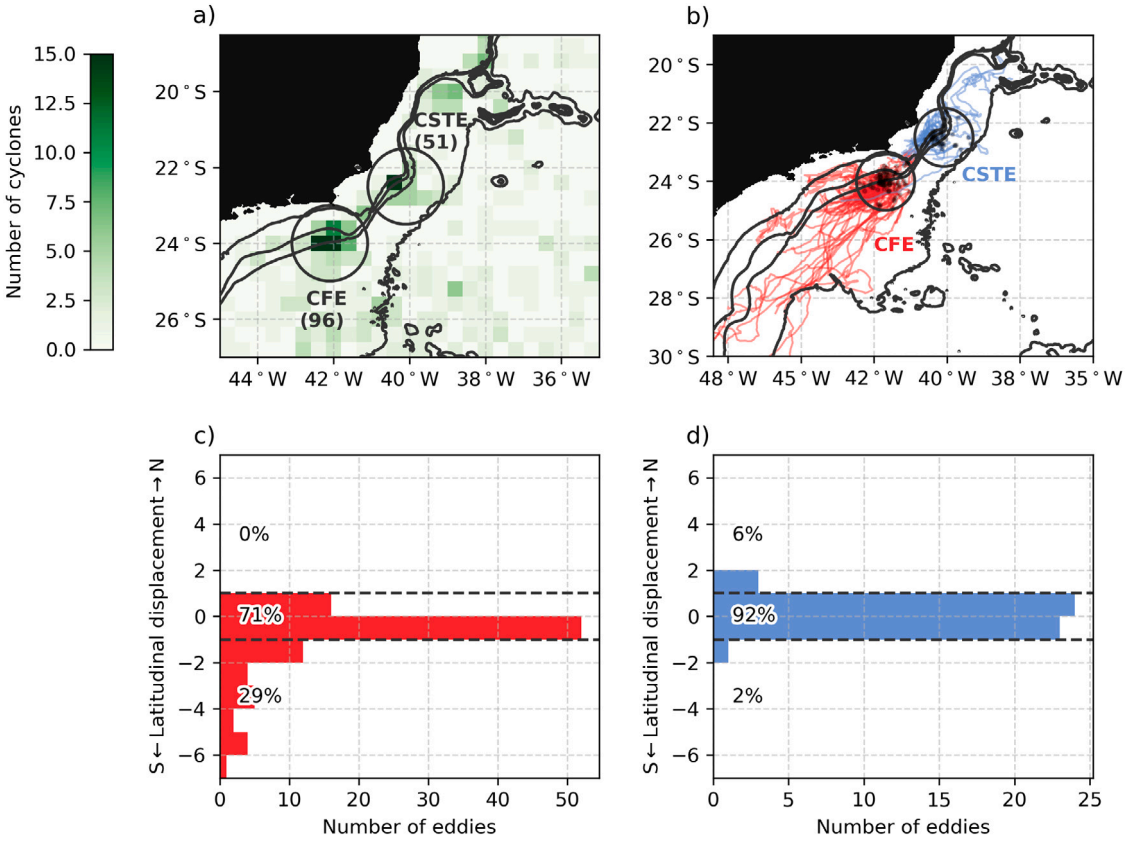

Fig. 4. (a) Map of occurrence of cyclones from the META3.1exp product. Black contours are the 100, 1000 and 3000-m isobaths. (b) Trajectories for Cape Frio Eddies (CFE) in red and Cape São Tomé Eddies (CSTE) in blue. Histograms for the CFE and CSTE latitudinal displacements (final minus initial latitudes).

topography (ADT) instead of Sea Level Anomaly (SLA) for eddy identification which better describes ocean dynamics near boundaries since we expect the BC eddies under study to emerge around local topographic features.

The META3.1exp provides specific characteristics for the tracked eddies, such as the amplitude, center position, radius, and average swirling speed. We here consider the effective eddy radius, which is estimated from the outermost sea surface height closed contour, and we also computed the eddies' lifetime. We removed from the analyses eddies with a maximum amplitude smaller than 5 cm and generated over the continental shelf (local depth shallower than 150 m), where we expect higher errors due to the influence of tidal sea level oscillations.

We categorize CF eddies (CFE) and CST eddies (CSTE) as the events generated within 1° (~112 km) from the peak of cyclone's formation frequency near each cape (Fig. 4a). We identified a total of 96 CFE (~3.5 year^{-1}) and 51 CSTE (~1.8 year^{-1}). Despite the complex migration shown by the eddy trajectories (Fig. 4b), most of the CFE (~71%) and CSTE (~92%) events remained within 1° of their birth site. Even so, about 29% of the CFE events detach and propagate southwestward (Fig. 4c, d).

Approximately 6% of CSTE events travel northward, and only 2% of the events migrate southward. CFE are more migrant and last considerably longer than CSTE (Fig. 5a, b), with lifetimes spanning 24–97 days, while CSTE events last for 15–46 days (20th and 80th percentiles). On

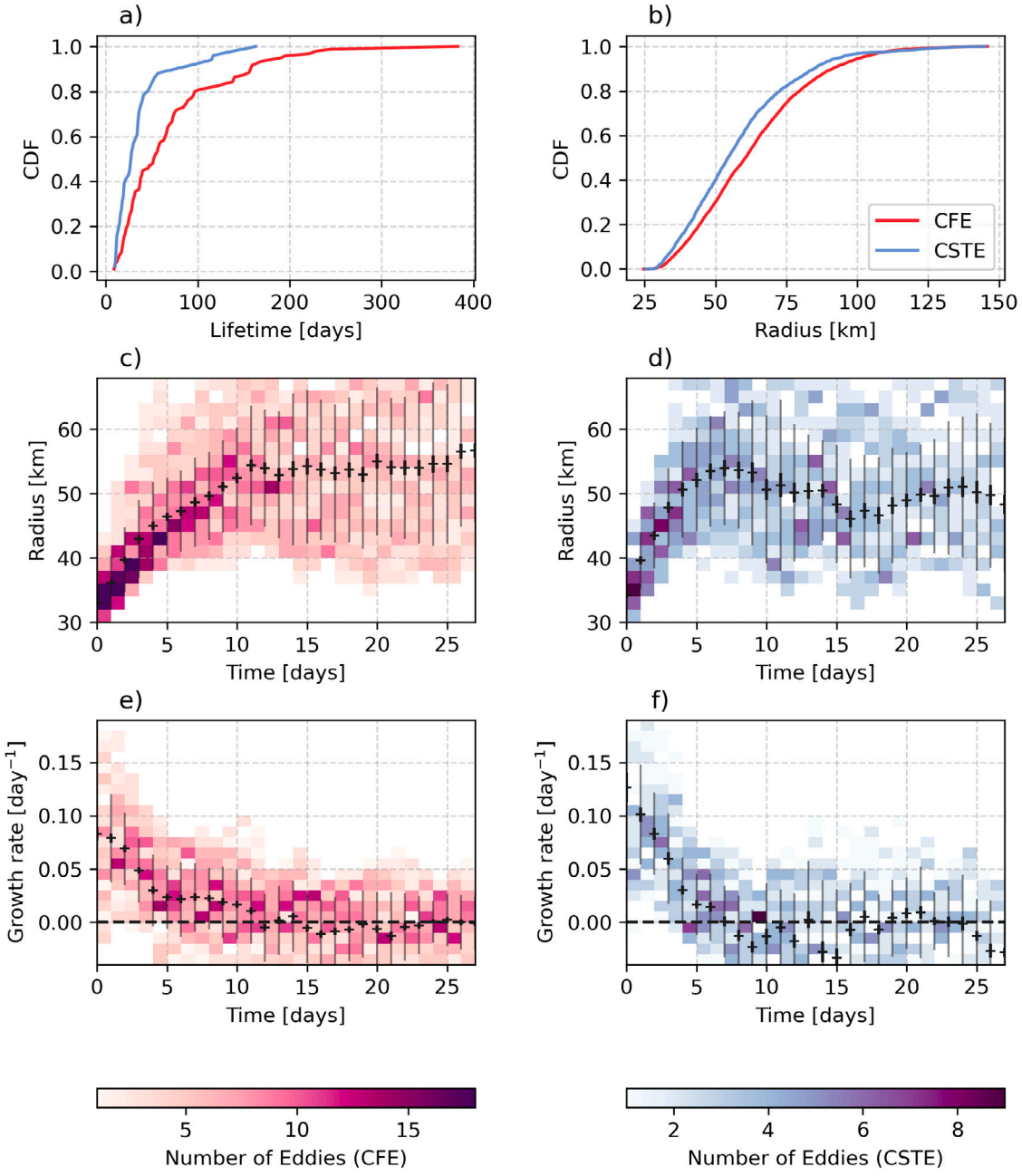

Fig. 5. Cumulative density functions for (a) eddy duration and (b) radius. Red lines are for Cape Frio Eddies (CFE), and blue lines are for Cape São Tomé Eddies (CSTE). Mean radius and joint histograms (colors) for (c) CFE and (d) CSTE. Mean growth rate $\sigma = {}^{d}/_{dt}\ln(\text{radius})$ and joint histograms (colors) for (e) CFE and (f) CSTE. The long thin error bars represent standard deviations, and the shorter, thicker ones standard errors.

average, CFE lasts for 71 days and CSTE for 37 days. The CFE is also slightly larger (radius of 44–80 km) than the CSTE (radius of 40–72 km, 20th and 80th percentiles). CFE and CSTE radii grow significantly in the first 10 days after detection, approximately, and then reach a stable averaged radius whose variations are not significant with time. CSTE grow faster and reach similar sizes as CFE but become slightly smaller after 10 days (Fig. 5c, d).

We estimate growth rates from the detected eddy contours by simply taking $\sigma = {}^{d}/_{dt}\ln(\text{radius})$. The CFE and CSTE have similar maximum average growth rates of 0.1 day^{-1}, while CFE events seem to grow for a longer period (Fig. 5e, f). The growth rate decays exponentially in the first 14 days (three times the *e*-folding scale) for CFE and the first 8 days for CSTE. For the first five days, both eddies grow approximately 0.06 day^{-1} on average. Although there is no significant difference in the maximum and average values between CFE and CSTE, all SSH-estimated growth rates are within the range of our SST-based estimates. Despite the small mean *e*-folding scale, some of the eddies could grow more slowly for longer periods. For instance, the examples of quasi-stationary growth depicted in Fig. 6 occur during approximately 30 days, with an average growth rate of 0.02 day^{-1}.

2.3. Reconciling the SST and SSH results

We found a 0.7 year^{-1} frequency for CFE and 0.5 year^{-1} for CSTE with the SST analysis, whereas with the SSH analysis, a frequency of 3.5 year^{-1} for CFE and 1.8 year^{-1} for CSTE. Indeed, Mill et al. (2015) found an average frequency of 2.5 year^{-1} for CSTE (22 eddies from 2003 to 2013), they employed SLA data using a different eddy detection method.

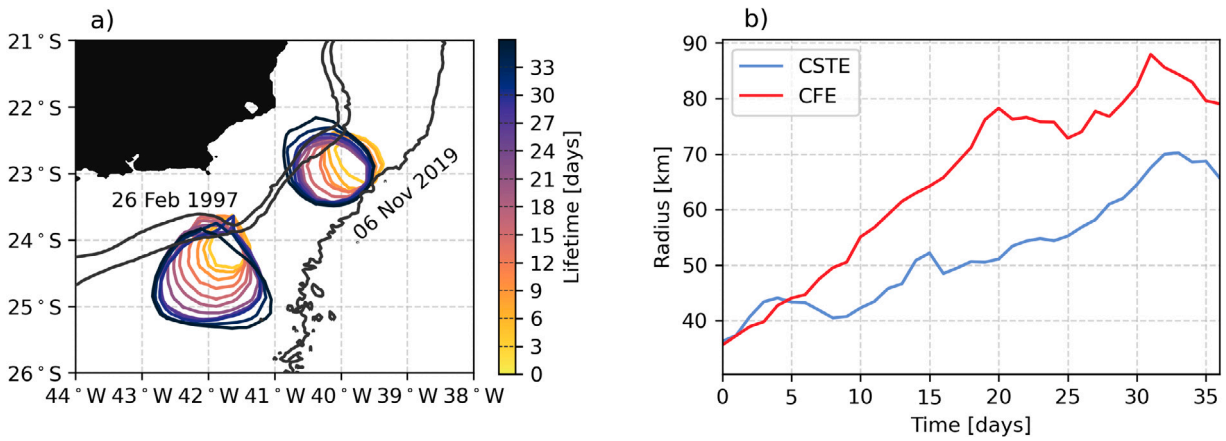

Fig. 6. (a) Examples of quasi-stationary growth of the Cape Frio Eddy and the Cape São Tomé Eddy. The eddy contours are spaced by 3 days. (b) The eddy radius timeseries for the first 35 days of each event.

Although CFE migration episodes have been previously documented in the literature using mooring and altimetry data (Guerra et al., 2018), our finding that 29% of CFE migrate southward supports earlier research that suggests the CFE grows mostly quasi-stationary, eventually necks off from the BC and propagates as an isolated ring (Calado et al., 2008; Silveira et al., 2008; Fernandes et al., 2009).

Mill et al. (2015) reported four northeastward (~18%) and only two southwestward (~9%) trajectories among the total 22 altimetry-observed CSTE between 2005 and 2013. Therefore, by using a longer time series and automated eddy detection, our results suggest that migration is even more occasional for CSTE cyclones (6% northward and 2% southward) (Fig. 4c, d).

The events shown in Fig. 2a, b, apparently corroborate the hypothesis that CST and CF meanders may be rationalized as troughs of a first-mode unstable vorticity wave train, as proposed by Silveira et al. (2008). The wavelength of ~220 km estimated from the SST images is also comparable to the values predicted by the linear baroclinic instability analyses of Silveira et al. (2008) and Rocha et al. (2014). These studies predicted wavelengths of ~260 km and ~230 km for the most unstable modes off CST, respectively.

The averaged growth rate of 0.1 day^{-1} estimated with the SST analysis is equal to the maximum averaged growth rate obtained with the SSH analysis. These values are comparable to theoretical predictions from previous studies. Specifically, the linear baroclinic instability analyses of Silveira et al. (2008) and Rocha et al. (2014) predicted growth rates (phase speeds) of 0.06 day^{-1} and 0.04 day^{-1} for the most unstable wave modes, respectively.

However, we should emphasize that predictions from linear baroclinic instability models should be most relevant to the early growth stages of the observed cyclones, since finite-amplitude nonlinear effects may be expected to dominate later. In this regard, the SSH-derived growth rate of 0.06 day^{-1} (averaged in the first 5 days) is comparable to the predicted growth rates found by Silveira et al. (2008) and Rocha et al. (2014).

We found average radii of 63 km for CFE and 57 km for CSTE with the SSH analysis. Mill et al. (2015) estimated the mean CSTE ring radius as 55 ± 9 km from altimetry data. *In situ* measurements are seldom, but previous quasi-synoptic vertical sections have shown that the CFE and CSTE cyclones have radii of about 54 km and 48 km, respectively (Silveira et al., 2004, 2008).

Despite the differences of the two methods employed, the parameters obtained converge, falling in the same range. However, we should point out their limitations. Firstly, in using the cross-stream position of the SST front to estimate growth rates, no distinction is made between the cross-stream displacement of the entire BC jet and actual meander growth, i.e., the amplitude increase. Moreover, the MUR product provides daily images but there is an important loss of resolution when microwave imagery is merged to the final product during cloud-covered periods. The result of the exponential fitting becomes, therefore, sensitive to the choice of images in each event. For these reasons, we interpret the SST-derived growth rates with more caution than the growth rates derived with the fully automated SSH imagery processing. On the other hand, we are aware of the SSH analysis limitations imposed by the smoothing of the Level 4 ADT product (Ballarotta et al., 2019). Additionally, a manual inspection of the images in each event was necessary in the SSH analysis, given that the scheme does not distinguish meanders from rings, and therefore does not identify the time of eddy shedding. Also, this is the reason we opted not to estimate propagation speeds from SSH images when the eddy is still attached to the BC.

3. Evidence of baroclinic growth from *in situ* observations

In this section, we approximate the scenario captured by the "Oceano Sudeste IV" (OSE4 for short) hydrographic survey off the Two-cape Region with a two-layer QG ocean to seek evidence of layer interaction and resulting baroclinic growth. We closely follow Silveira et al. (2000) on this matter. These authors used a three-layer approximation of the North Brazil Current retroflection region captured during the Western Tropical Atlantic Experiment to search for instability mechanisms. They created a simple potential vorticity (PV) inversion model, and analyzed whether the vortical features in each of the three layers interact and induce growth on the other two through vortex stretching and squashing.

3.1. The data set

We use original hydrographic data from the OSE4 expedition conducted by the Brazilian Navy's R/V Antares between 2006/01/27 and 2006/04/24. The measurements consisted of vertical profiling using a CTD profiler and shipboard Acoustic Doppler Current Profiler (ADCP).

A Sea-Bird Electronics SBE 9 Plus CTD was employed in the hydrographic measurements. The instrument was set to collect data using a sampling frequency of 24 Hz. Its temperature, pressure and conductivity sensors were calibrated on 2005/10/13 in the Oceanographic Instrumentation Calibration Center at the University of São Paulo. The locations of the CTD stations are indicated by the white dots in Fig. 7.

The shipboard 75 kHz RDI ADCP profiled the upper ocean continuously along the ship track, and near-surface (32 m) velocity vectors are indicated in Fig. 7. The ADCP, which was configured for 8 m bins, reached a depth range of about 400 m. We employed the *Common Ocean Data Access System* (CODAS) software (*e.g.*, Firing and Hummon, 2010), developed by the University of Hawaii, to process the raw data and obtain absolute velocities.

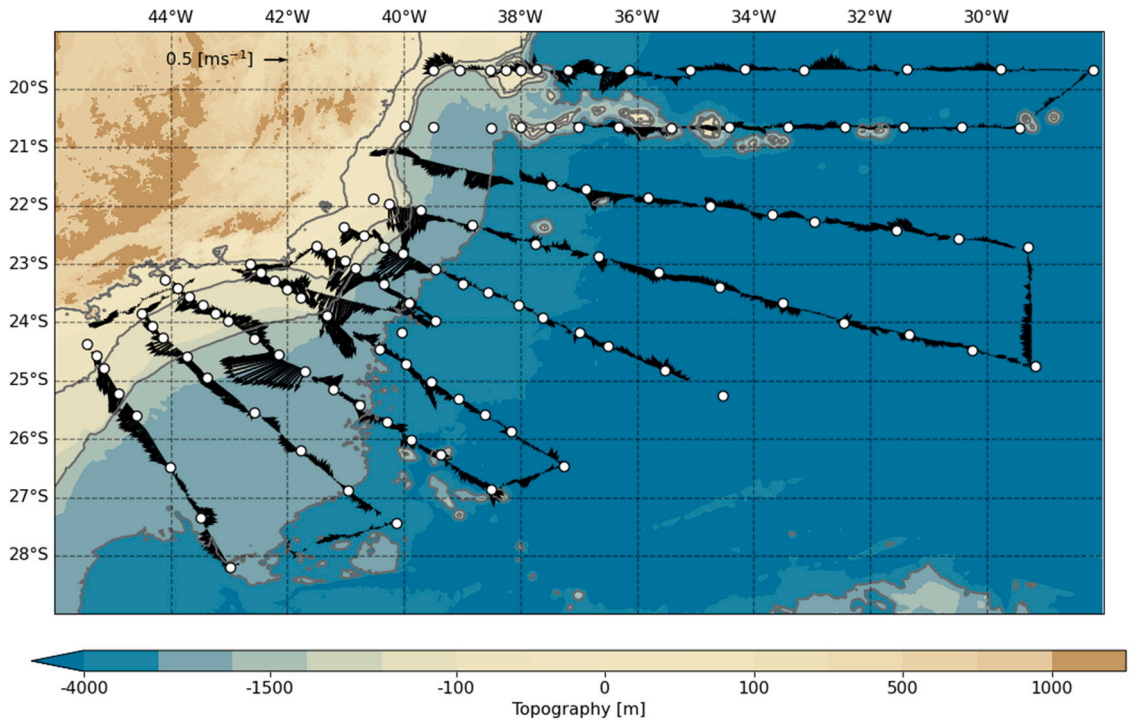

Fig. 7. The Oceano Sudeste IV survey grid. The white dots show the locations of the CTD stations. Velocity vectors at the 32 m depth measured by the 75 kHz shipboard ADCP are displayed along the ship track. No ADCP data was available on the transect at ~20.5°S between 40°W and 37°W. The color scale represents bottom topography obtained from GEBCO 2021.

3.2. Near-surface geostrophic stream function maps

Before we proceed building the two-layer model using the quasi-synoptic observations, we should consider two aspects of using the OSE4 data set. First, we do acknowledge that the cruise sampling period (45.5 days) was large compared to the average estimated growth rates of about 0.06 day^{-1} (that is, the meander doubles its amplitude in two weeks). Therefore, the synopticity of the data must be checked to verify if the growth is captured in at least one of the two eddies before it ceased.

The second is the fact that, for depths below 200 m, the ADCP had low percent good values (quality), in spite of viable data being usually available at least in the upper 500 m for a 75 kHz instrument. As the ADCP data was too shallow to be employed to reference the classical dynamical method (Biló et al., 2014), and to apply it to the IWBC, we opt to use an arbitrarily-chosen isopycnal as level of no motion. This isopycnal is chosen to be the one commonly taken as the mean interface between the SACW and AAIW: σ_θ=26.9 kg m^{-3} (Stramma and England, 1999; Mémery et al., 2000). This isopycnal, therefore, can be thought of as approximately marking the velocity inversion that separates the BC and IWBC domains (see Fig. 1b).

In order to address these two concerns, we perform a calculation to evaluate the synopticity of the cruise data, as well as the validity of using the geostrophic fields based on a fixed level of no motion relatively to the observed velocity data. We compare geostrophic velocity fields obtained by different instruments: (1) near-surface geostrophic velocities calculated using the OSE4 CTD data (Fig. 8a), (2) the near surface, horizontally nondivergent velocities derived from the OSE4 ADCP data (Fig. 8b), (3) the averaged altimeter-derived geostrophic velocities (Fig. 8c). Fig. 8d shows the standard deviation over the OSE4 period. Of course, the comparison between (1) and (2) addresses how adequate our geostrophic calculation is, despite the ageostrophic component in (2) and different errors in mapping. The comparison between (1) and (3) allows a check on how the degree of synopticity of the *in situ* data distorted the velocity fields relatively to a mean of truly synoptic fields derived from satellite imagery. The standard deviation map illustrates the growth of the meanders during the OSE4 period.

The geostrophic stream function ψ is calculated as

$$\psi = \frac{\Delta\Phi}{f} = \frac{1}{f}\int_p^{p_0} \delta_\alpha(x, y, p')\, dp' , \tag{1}$$

at each oceanographic station, where $\Delta\Phi$ is the geopotential anomaly, f is the Coriolis parameter evaluated at 23°S, δ_α is the specific volume anomaly, and p_0 = 520 dbar, the averaged isobaric level of σ_θ within the study area.

The horizontal mapping of the geostrophic stream function is conducted using an optimal interpolation scheme following Silveira et al. (2000). The scalar objective analysis (OA) considers a decorrelation length of 90 km, and Dirichlet boundary conditions. The ADCP-derived stream function required the vector OA technique (Bretherton et al., 1976). We use the same decorrelation length and Neumann boundary conditions. The objective maps are constructed on a 1/10° resolution grid.

Fig. 8 displays the three ψ fields obtained with the CTD, ADCP and altimetric data from AVISO+. A first inspection yields a scenario where both CFE and CSTE are well developed. In the average of the three fields, the CFE and CSTE have diameters of 165 km and 72 km, respectively, which represents a picture that agrees well with the average results described in Section 2. The ADCP- and the CTD-derived geostrophic fields (Fig. 8a, b) are similar, but while the maximum azimuthal velocity of the CFE is 0.35 m s^{-1} in the ADCP field and 0.29 m s^{-1} in the CTD field, the CSTE has a maximum azimuthal velocity of 0.11 m s^{-1} in the ADCP field and 0.23 m s^{-1} in the CTD field. There seems to be good agreement between the eddy positions, the CFE (CSTE) is centered at 42.4°W-23.6°S, 42.5°W-24.1°S, 42.3°W-24.3°S (40.5°W-22.5°S, 40.3°W-22.4°S, 40.4°W-22.5°S) in the CTD, ADCP and AVISO+ fields, respectively. These simple results encourage us to pursue the layer interaction calculation. Fig. 8d shows twice as much variability in the CFE region, due to its shedding during the cruise. We will focus our analysis on the CSTE, which seems to have started growing during the OSE4 survey period.

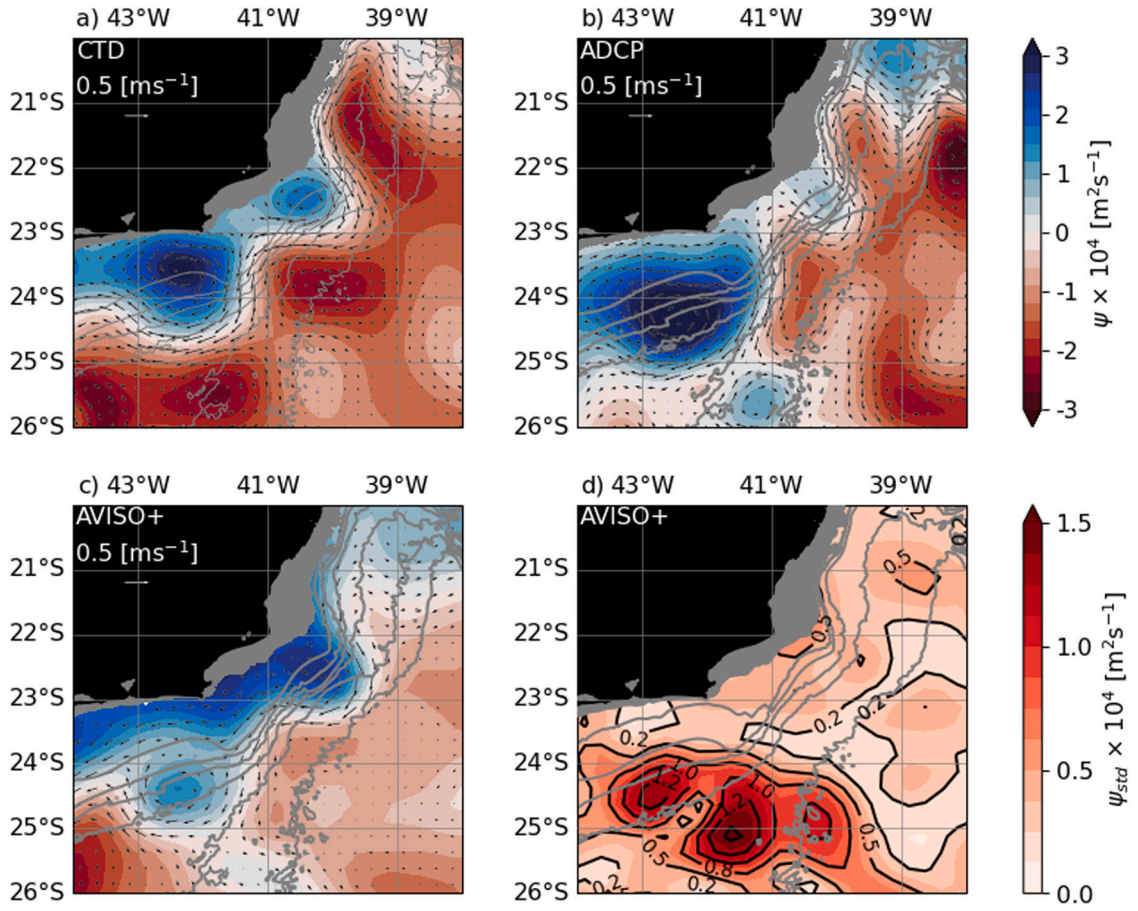

Fig. 8. Comparison among the near-surface stream function fields of the Oceano Sudeste IV expedition derived from (a) the dynamic method using CTD profiles (at 32 m); (b) the shipboard ADCP profiles (at 32 m); (c) the average of AVISO+ altimetry data between 2006/01/28 and 2006/03/21. (d) The standard deviation of AVISO+ altimetry data between 2006/01/28 and 2006/03/21. Gray contours are the 200 m, 1000 m, 1500 m, 2000 m, 2500 m and 3000 m isobaths.

3.3. The two-layer, quasi-geostrophic approximation

Now we develop the theoretical framework, which we will use to construct the two-layer approximation to the BC-IWBC system. The BC (IWBC) occupies the upper (lower) layer in a QG ocean on the f-plane. The velocity in each layer is diagnosed from the geostrophic stream function ψ_i: $[u_i, v_i] = [-\partial_y, \partial_x]\,\psi_i$. The layer potential vorticity q_i relates to ψ_i via

$$\begin{aligned} q_1 &= \nabla^2\psi_1 - \frac{\alpha_2}{{R_d}^2}(\psi_1 - \psi_2)\,, \\ q_2 &= \nabla^2\psi_2 - \frac{\alpha_1}{{R_d}^2}(\psi_2 - \psi_1)\,, \end{aligned} \tag{2}$$

where

$$R_d = \frac{\sqrt{g' H_m}}{|f|} \tag{3}$$

is the baroclinic deformation radius, with the reduced gravity $g' = g(\rho_2 - \rho_1)/\rho_0$ and harmonic-mean thickness $H_m = \alpha_1\,\alpha_2/(\alpha_1 + \alpha_2)$. Also in (2), $\alpha_i = \alpha_i/(\alpha_1 + \alpha_2)$ is the aspect layer of the ith layer.

In dynamical-mode space, the inversion relationships between the modal potential vorticity Q_j and the modal stream function Ψ_j become

$$\begin{aligned} Q_0 &= \nabla^2\Psi_0 \\ Q_1 &= \nabla^2\Psi_1 - \frac{1}{R_d^2}\,\Psi_1\,, \end{aligned} \tag{4}$$

where the indices 0 and 1 refer to the zeroth (or barotropic), and the first (or first baroclinic) modes, respectively.

The relationships between the layer and modal quantities are

$$[\Psi_j, Q_j] = \sum_i \alpha_i\, F_i^j\,[\psi_i, q_i]\,, \tag{5}$$

where F_i^j represents the amplitude of the jth dynamical mode onto the ith layer given by

$$\begin{aligned} &F_1^0 = F_2^0 = 1 \\ &F_1^1 = \sqrt{\frac{\alpha_2}{\alpha_1}} \quad \text{and} \quad F_2^1 = -\sqrt{\frac{\alpha_1}{\alpha_2}}\,. \end{aligned} \tag{6}$$

The baroclinic growth problem can be thought of as an evidence of baroclinic instability. In other words, the potential anomalies in one layer can interact in a way that enhances the anomalies in the other layer. Of course, having a single quasi-synoptic snapshot, captured during the OSE4 cruise, we are unable to separate mean fields and anomalies. We ask the reader to interpret the derivation and analysis that follows in a broader sense: the PV contours in each layer interact and their mutual enhancement can be detected by examining regions where the Jacobian $J(\psi_i, q_i) = \vec{k}\cdot\left(\nabla\psi_i \times \nabla q_i\right) \neq 0$.

The modal inversion relations in (4) are linear and we can split the jth modal stream function in three parts:

$$\Psi_j = \Psi_j^{(1)} + \Psi_j^{(2)} + \Phi_j\,, \tag{7}$$

where $\Psi_j^{(k)}$ is the jth modal interior domain stream function due to anomalies on the kth layer *only*, and Φ_j is the jth modal boundary stream function. The jth modal stream function in (7) relates to the jth modal potential vorticity via

$$\left(\nabla^2 - \frac{\delta_{1j}}{R_d^2}\right)\Psi_j^{(k)} = Q_j^{(k)} \qquad \text{with} \qquad \Psi_j^{(k)} = 0 \quad \text{at the boundaries}\,, \tag{8}$$

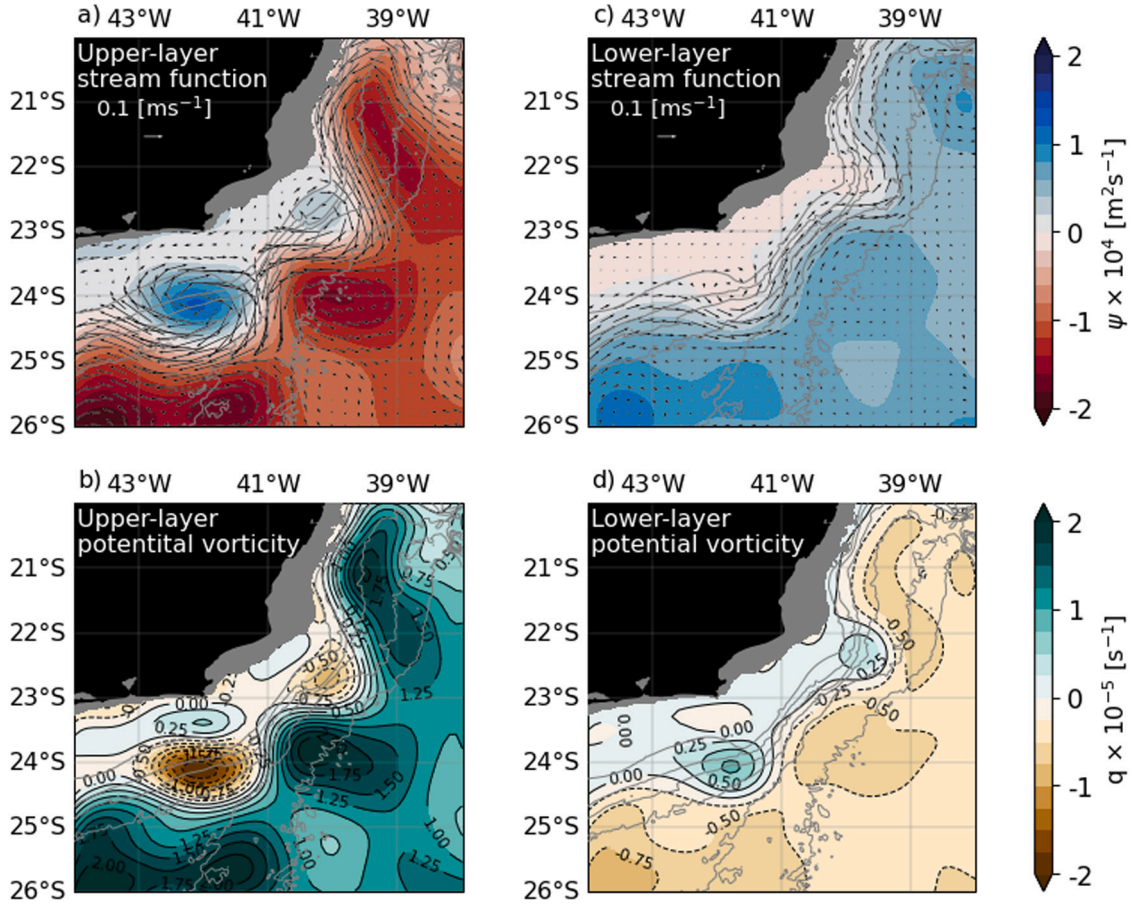

Fig. 9. The Oceano Sudeste IV two-layer fields: QG stream functions (ψ_i), velocities and potential vorticities (q_i) for (a), (b) i=1, and for (c), (d) $i = 2$. Gray contours correspond to the 200 m, 1000 m, 1500 m, 200 m0, 2500 m and 3000 m isobaths.

and

$$\left(\nabla^2 - \frac{\delta_{1j}}{R_d^2}\right)\Phi_j^{(k)} = 0 \qquad \text{with} \qquad \Phi_j^{(k)} = \Psi_j \quad \text{at the boundaries}. \tag{9}$$

In (8), $Q_j^{(k)}$ represents the jth modal PV field due to the PV structure in the kth layer only, that is,

$$Q_j^{(k)} = \alpha_k\, q_k\, F_k^j \tag{10}$$

for $j = 0, 1$ and $k = 0, 1$. Note also that δ_{jk} represents the Kronecker delta function. We solve (8) and (9) by numerical iteration, and recover the layer quantities using

$$[\psi_i, q_i] = \sum_j F_i^j [\Psi_j, Q_j]. \tag{11}$$

3.4. The two-layer fields

In order to approximate the real continuously stratified ocean with a two-layer, QG ocean, we need to estimate the layer aspect ratios δ_i and the baroclinic deformation radius R_d. The ith layer stream function fields can be obtained by simply averaging the geostrophic stream function mapped at every 10 m from the OSE4-derived dynamic topography.

However, it is necessary to choose the rest thicknesses of each layer (i.e., α_1 and α_2) in order to delimit the depth range to be considered in the averaging process. In addition, we also need to infer the deformation radius, which by (3) is equivalent to estimating the normalized density jump $(\rho_2 - \rho_1)/\rho_0$.

3.4.1. Two-layer calibration

We adopt H=1800 m as the model total depth. Hence, we are essentially truncating the model depth to the lower limit of the intermediate continental slope. We choose α_1 to coincide with the mean depth of σ_θ, which is an acceptable reference for the SACW-AAIW interface (see Stramma and England, 1999). From the OSE4 data set, we estimate this isopycnal to be at roughly 500 m depth over the continental slope of the Two-cape Region. Hence, the values of $\alpha_1 = 0.28$ and $\alpha_2 = 0.72$ are employed.

We apply the concepts of the classical layer model calibration scheme originally proposed by Flierl (1978), but we choose α_1 and α_2. We here impose the model baroclinic deformation radius to be equal to the continuously stratified first baroclinic deformation radius. Using the OSE4 mean hydrographic profile, we compute the first baroclinic deformation radius R_d = 33 km, and use it to calibrate the two-layer QG model. Having α_1, α_2, and R_d, we find $(\rho_2 - \rho_1)/\rho_0 = 9.6 \times 10^{-4}$ (3). The Coriolis parameter f is calculated at the central latitude between the Capes São Tomé and Frio: 22.5°S.

3.4.2. The OSE4 two-layer fields

We constructed the layer fields on a 1/10° resolution grid, considering the 150 m isobath as a vertical wall separating land and ocean. We apply OA to the stream function mapped using Dirichlet boundary conditions, according to the same protocol described in Section 3.2. The PV fields were computed using (2).

Fig. 9 displays the fields obtained for the layer stream function and potential vorticity. The upper layer ψ field portrays a meandering BC very similar to the near-surface field presented in Fig. 8; both the CFE and the CSTE are well developed, and surrounded by anticyclones. The lower field exhibits the IWBC, flowing opposite and with maximum

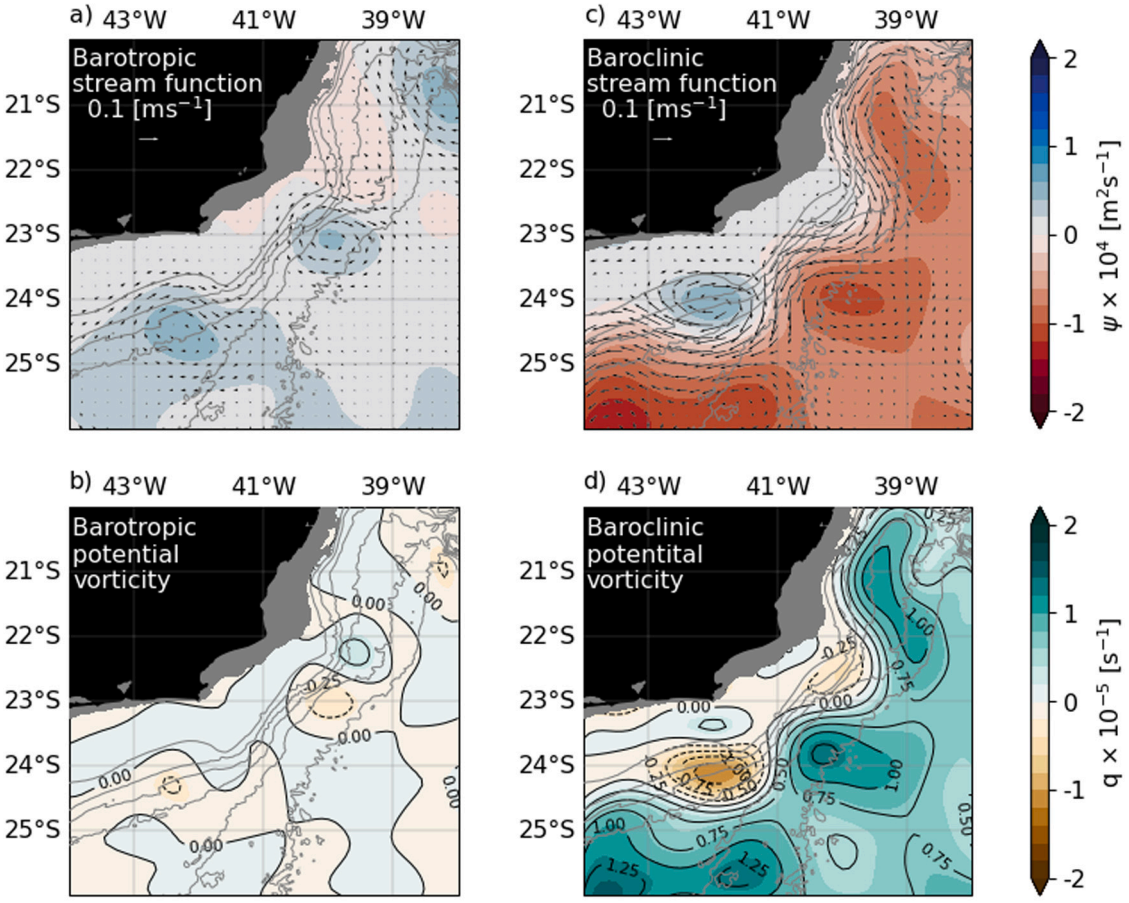

Fig. 10. The Oceano Sudeste IV modal fields: QG stream functions (Ψ_j), velocities and potential vorticities (Q_j) for (a), (b) j=0, and for (c), (d) $j = 1$. Gray contours are the 200 m, 1000 m, 1500 m, 2000 m, 2500 m and 3000 m isobaths.

speeds of about one-third of the upper layer ones. There are weaker anticyclonic features representing the lower layer signatures of both CFE and CSTE. The q fields are similar in pattern to their ψ counterparts and PV contours are closed around the two cyclones. Note also the lower layer cyclone depicted at 21°S. This feature probably corresponds to the steady IWBC recirculation described by Costa et al. (2017) and Napolitano et al. (2019), which is bounded to the north by the Vitória-Trindade Ridge (20.5°S). Another conspicuous feature is the elliptical anticyclone centered at 39°W in Fig. 9a, c, which has been called the South Vitória Eddy (SVE) (Arruda et al., 2013; Arruda and Silveira, 2019). Overall, we can state that the two-layer approximation captures the BC and IWBC domains and their associated vortical activity adequately.

We also compute the zeroth and first modal amplitude maps of ψ and q by employing (5). The modal fields also provide interesting insight (Fig. 10). We see that most of the features are well represented in the baroclinic fields, including the BC-IWBC jet. On the other hand, the barotropic field is dominated by the cyclones: the CFE and the CSTE. We find no signature of the jet in the barotropic field, i.e., the BC-IWBC jet is dominantly baroclinic, while the meanders contain a relevant barotropic component. This result is consistent with the remarks presented by Silveira et al. (2004, 2008) and Rocha et al. (2014).

3.5. Layer interactions

In this section, we present the results of the layer interaction analysis conducted in the OSE4 two-layer fields. These interactions should be interpreted as arising from the perturbations in the q_i contours in several areas that may indicate tendency of growth and/or mere advection of the anomaly up or downstream. More specifically, the anomaly in one layer causes the anomaly in the other layer to amplify, and vice-versa. We should re-emphasize that, for the current analysis, a steady-state for the BC-IWBC jet is unknown and cannot be inferred from the OSE4 quasi-synoptic snapshot. Besides, by PV "anomaly" we mean areas where PV isolines are not parallel to the streamlines. This is because, in the case of a steady state ($\partial_t q_i = 0$),

$$J\left(\psi_i, q_i\right) = |\nabla\psi_i|\,|\nabla q_i|\sin(\gamma) = 0\,, \tag{12}$$

where γ is the angle between the gradients of stream function and PV. Hence, the PV isolines will evolve only if not parallel to the streamlines.

Additionally, as pointed out by (7), we have split the stream function field into an ith-layer boundary (ϕ_i) and an ith-layer interior $\left(\sum_j \psi_i^{(j)}\right)$ components. This splitting is rather convenient because it allows us to separate the ith-layer interior stream function in two parts: the flow associated with PV anomalies in the same layer ($i = j$), and due to PV anomalies in the other layer ($i \neq j$). The advantage is that we do not have to deal with inhomogeneous boundary conditions (8) for the interior part of the solution. However, this split is only valid for the interaction analysis if the anomalies extend toward the ocean interior.

Fig. 11 exhibits the Jacobian of total and partial interior stream function components with PV isolines, as shown in (12). The purple (blue) patches indicate advection out of the eddy in the upper (lower) layer; the green (golden) patches indicate advection in the opposite direction (i.e., into the eddies) in the upper (lower) layer. Panels (a) and (d) display the total interior stream function. It is evident that advection is far more vigorous at the CFE and CSTE edges, indicating these are the locations where PV contour motion is more likely to occur.

The advection of the q_1 (q_2) contours by the partial stream function $\psi_1^{(1)}$ ($\psi_2^{(2)}$) indicates that the meanders tend to grow. Since we are

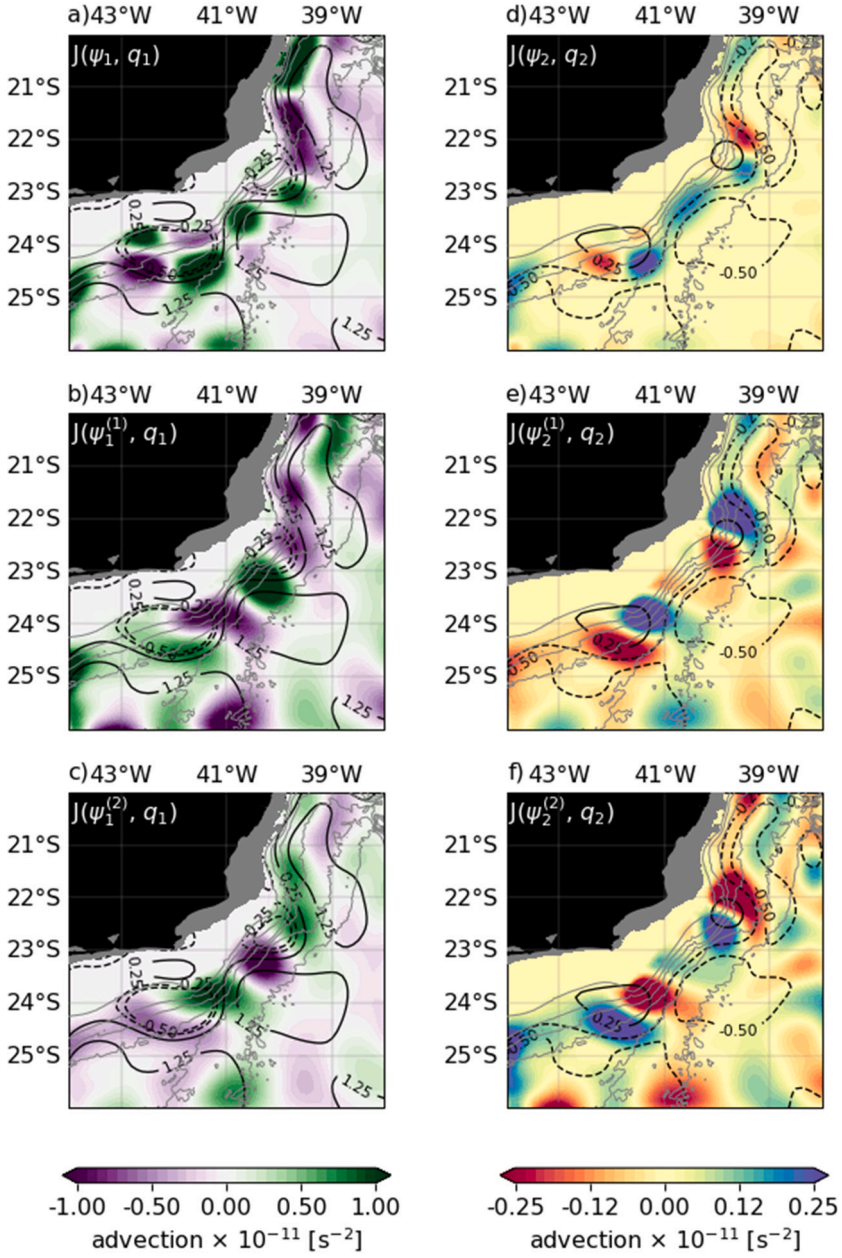

Fig. 11. The $J(\psi_i, q_i)$ fields regarding the advection of ith layer PV contours by the split stream function fields: (a) upper layer total interior stream function, (b) the upper layer interior stream function due to PV anomalies in the layer itself, (c) the upper layer stream function due to PV anomalies in the lower layer, (d) the lower layer total interior stream function, (e) the lower layer interior stream function due to PV anomalies in the upper layer, and (f) the lower layer. The purple (blue) patches indicate advection out of the eddy in the upper (lower) layer; the green (golden) patches, advection into the eddy in the upper (lower) layer. Gray contours correspond to the 200 m, 1000 m, 1500 m, 2000 m, 2500 m and 3000 m isobaths.

dealing with advection by currents generated by the PV anomalies occurring in same layer, this growth may be indicative of barotropic, rather than baroclinic processes (Fig. 11b, f). However, there is evidence of baroclinic growth in the advection due to $\psi_1^{(2)}$ and $\psi_2^{(1)}$, which indicate flow in one layer generated by the presence of PV anomalies present in the other layer. The patches oppose each other in terms of circulation, and we observe them somewhat displaced in the vertical. This displacement causes the q_i anomalies in one layer to induce currents on the other layer, mutually reinforcing growth (Fig. 12).

Silveira and Flierl (2002) used simple theoretical models to explain that the PV anomaly vertical displacements cause the release of potential energy and start/maintain the process of baroclinic instability. That is the scenario captured during the OSE4 campaign. Additionally, Mano et al. (2009) used a primitive-equation model to simulate the CFE, verifying that the meander growth's primary mechanism is indeed baroclinic instability. According to these authors, barotropic instability does occur after the meander has grown significantly. Our analysis clearly shows baroclinic growth, however, this is just a quasi-synoptic snapshot of the process. We need to understand the evolution of the growing quasi-stationary meanders and we will do so by using process-oriented modeling.

4. Assessing the meanders' quasi-stationary growth using the contour dynamics technique

We choose a minimalist dynamical model to investigate the quasi-stationary meanders of the BC-IWBC jet. We assume that baroclinic instability is the leading-order mechanism for meander growth. Despite

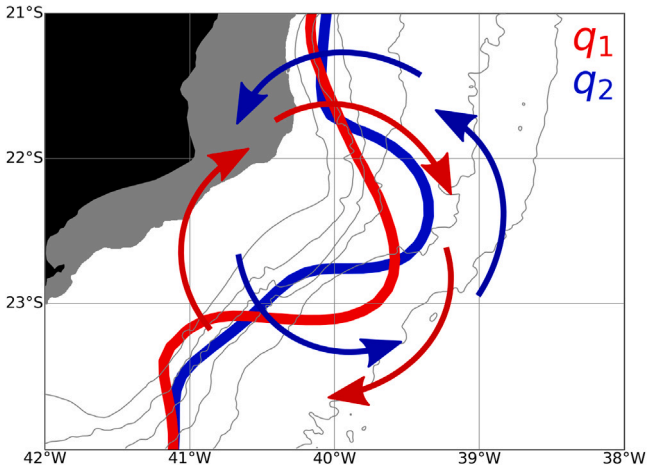

Fig. 12. The Cape São Tomé Eddy baroclinic growth. The red (blue) solid line represents the central PV contour of the BC-IWBC jet in the upper (lower) layer. The arrows represent the circulation generated by the PV anomaly due to the meander in each layer, where reciprocal reinforcement occurs. Gray contours correspond to the 200 m, 1000 m, 1500 m, 2000 m, 2500 m and 3000 m isobaths.

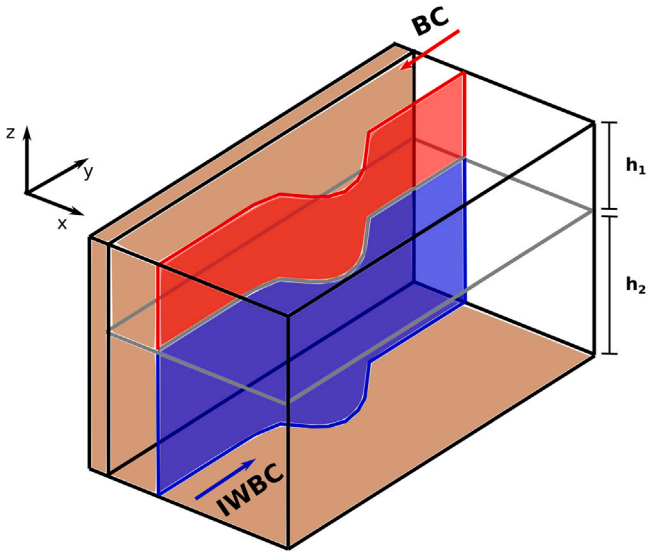

Fig. 13. The contour dynamics model setup for the BC-IWBC jet with flat bottom and a western vertical wall mimicking the continental slope. The horizontal field of potential vorticity (PV) and the density structure are discretized as piecewise-constant distributions. In the case of the PV field, the model presents one front in each layer, for the upper layer in red of thickness h_1 and for lower one in blue of thickness h_2. The fronts concentrate the dynamics of the approximated BC-IWBC system.

primarily addressing the first-baroclinic-mode structure of the mean BC-IWBC jet, we briefly explore the dynamical consequences of adding a barotropic component to the mean jet.

4.1. Configuration

The model chosen is an adaptation of the theoretical model developed by Meacham (1991) (hereafter M91) in a QG framework based on the contour dynamics (CD) method (Zabusky et al., 1979). M91 explored a double-PV front in a two-layer ocean, i.e., one front per layer. A piecewise-constant distribution approximates the potential vorticity (PV) field.

In the M91 study, the mean jet has no barotropic component and flows within a laterally infinite ocean. The study of the linear stability properties and the nonlinear evolution of the jet were possible under the CD technique. The author's infinite jet developed quasi-stationary unstably-growing meanders when perturbed by an initial Gaussian-like meander. Due to its simplicity, we see the M91 jet model as a useful tool to investigate the baroclinicity of the BC-IWBC jet.

The model is inviscid, unforced, under the QG approximation on the f-plane, with top rigid lid, and flat bottom. The main modification to the original M91 model is the inclusion of a meridional[3] western boundary, which mimics the continental slope. The domain is rectilinear, as the simplicity of the model makes it difficult to deal with the presence of the two capes explicitly due to boundary condition issues (Fig. 13). The model employs the image effect to satisfy the condition of no-flow normal to the boundary. Hence, curved topographic features in the boundary would not allow this method to be applied.

We opt to implicitly include the effect of the capes by prescribing cyclonic perturbations as initial conditions. Such perturbations are intended to mimic the excursions of the mean BC front in the vicinities of the capes. Such excursions are likely to trigger the instability process since they represent the attempt of the jet to circumvent the capes, as shown by the 1993–2019 mean BC zero-vorticity contour in Fig. 14, calculated from the AVISO+ altimetry data set.

In terms of the PV structure of the ith layer, the M91 jet allows for two regions of constant PV separated by a discontinuity: the contour. In our formulation, we consider a semi-infinite ocean with the western

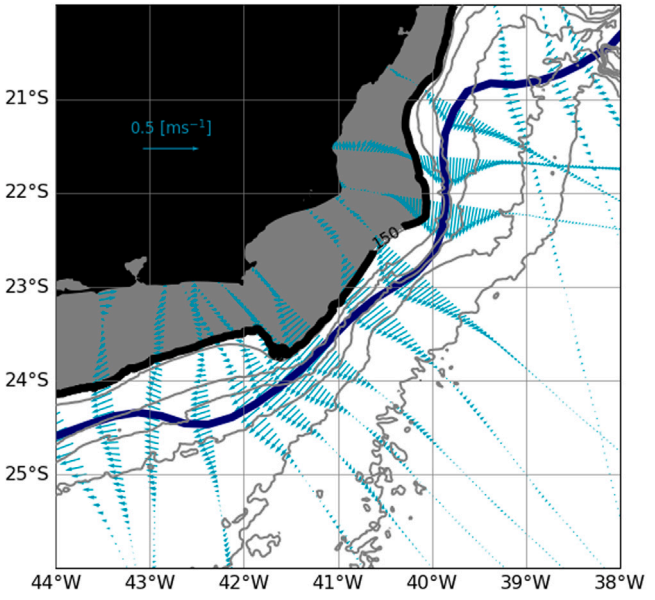

Fig. 14. The mean Brazil Current (BC) front. The dark blue curve characterizes the zero vorticity line along the BC axis and the vectors are the geostrophic velocities orthogonal to the axis for the 1993–2019 AVISO+ altimetry average. Notice that the front presents excursions off the Capes São Tomé and Frio, which may be associated with the recurrent formation of the quasi-stationary meanders. Gray contours correspond to the 200 m, 1000 m, 1500 m, 2000 m, 2500 m and 3000 m isobaths.

boundary located at $x = 0$ and the mean front located at $x = \bar{x}_i$. The expression for the ith-layer PV field is then given by

$$q_i = q_{0i} + \Delta_i \mathcal{H}(x - \bar{x}_i - \eta_i(y,t)) \,. \tag{13}$$

q_{0i} is the ith layer inshore PV value, Δ_i is the ith-layer PV jump across the front, $\eta_i(y,t)$ is the ith layer time-dependent front spatial deviations from the mean position $\bar{x}_i$, and $\mathcal{H}(x)$ represents the Heaviside step function. We will approach the instability problem of the M91 jet in two distinct ways:

[3] Despite the f-plane approximation, we choose to use a "georeferenced jargon" to refer to directions in the model for practicality.

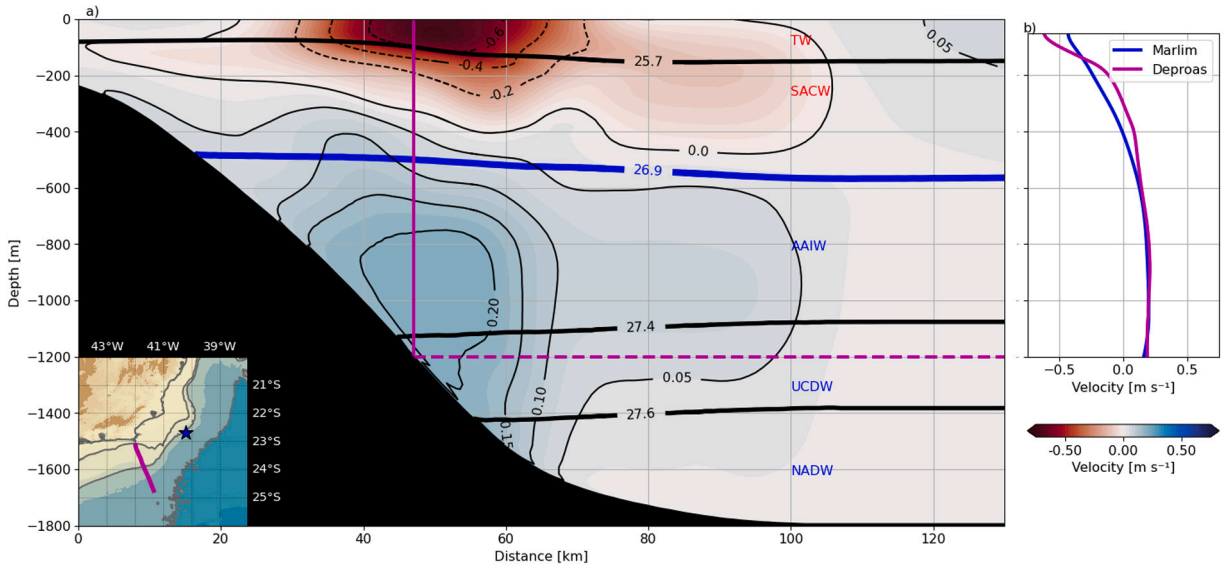

Fig. 15. (a) The numerically-generated velocity pattern of the DEPROAS5 transect (2003/09/28–2003/09/29). The westernmost station of the transect is located at (23.15°S, 42°W) and the easternmost one at (24.4°S, 41.5°W). The BC occupies the upper 400–500 m and the IWBC, the 500–1800 m depth range adjacent to the intermediate continental slope. The superposed isopycnals of 25.7 kg m^{-3}, 26.9 kg m^{-3}, 27.4 kg m^{-3} and 27.6 kg m^{-3} mark the TW-SACW, SACW-AAIW, AAIW-UCDW and UCDW-NADW interfaces. (b) Comparison between the vertical profiles of the section in magenta and the Marlim mooring alongshore velocity in blue. In both profiles, the local water column depth is of about 1200 m. The location of Marlim mooring and the DEPROAS5 transect are represented by the blue star and the magenta line on the map on (a), respectively.

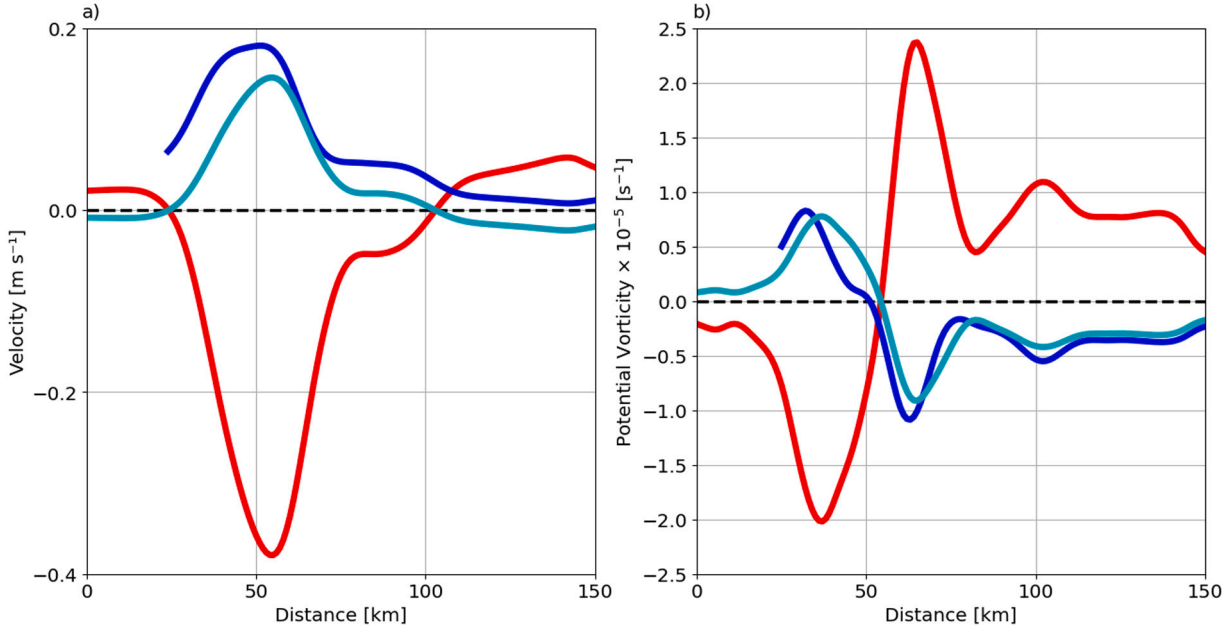

Fig. 16. The two-layer approximation to the DEPROAS5 transect. (a) the upper ($\tilde{v}_1$, red) and lower ($\tilde{v}_2$, blue) cross-isobath velocities. The cyan curve denotes the $-\frac{\delta_1}{\delta_2}\tilde{v}_1$ profile. (b) the upper ($\tilde{q}_1$, red) and lower ($\tilde{q}_2$, red) potential vorticity cross-isobath profiles. The cyan curve denotes the $-\frac{\delta_1}{\delta_2}\tilde{q}_1$ profile.

1. **Linear model** – Used to estimate the linear stability properties such as most unstable wavelengths, growth rates and phase speeds.
2. **Nonlinear model** – Used to evaluate the nonlinear evolution of the PV fronts in each layer and the associated velocity fields.

The reader will find more details on the mathematical formalism of the CD model in Appendix B.

4.2. The control run parameters

Let us now tune the model parameters to the BC-IWBC jet. We hereafter refer to this "tuning" and its application on both linear and nonlinear CD models as the *Control Run*. We consider a purely baroclinic jet configuration, such an assumption requires the mean PV fronts in each layer to be vertically aligned ($\bar{x} = \bar{x}_1 = \bar{x}_2$). The parameters to be chosen are then: the mean front position $\bar{x}$, and the upper-layer core velocity $\bar{v}_1(\bar{x})$.

4.2.1. Mean front position

The choice of $\bar{x}$ should reflect the average distance between the jet core and the western boundary in the study area. In such idealized configuration within the QG framework, we place the boundary at the shelf break and approximate the continental slope as a vertical wall. We estimate the mean distance between the shelf break and the mean

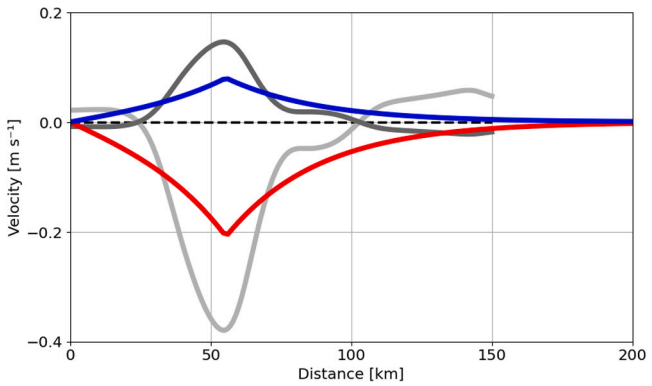

Fig. 17. Cross-boundary profile of the modeled alongshore velocity. The red (blue) curve refers to the upper (lower) layer jet. The jet volume transport in each layer is 6.8 Sv in opposite directions. The gray curves represent the two-layer approximation to the DEPROAS5 velocity section, same as red and cyan curves of Fig. 16.

BC front (Fig. 14). This distance is estimated to be 56 km on average (or $\bar{x} \approx 1.7\ R_d$).

4.2.2. Upper-layer core velocity

We should thus obtain a mean cross-stream profile of the BC-IWBC jet under the two-layer approximation from observations and fit the data to the theoretical expressions. We cannot build an average hydrographic section and calculate the mean geostrophic velocity pattern in the Two-cape Region from the OSE4 cruise. The meanders in Fig. 8 are well-developed and do not represent a probable mean flow.

We then opt to use an original quasi-synoptic transect sampled off CF during the Dynamics of the Shelf Ecosystem of the Western South Atlantic Region V (DEPROAS5, in Portuguese) cruise aboard University of São Paulo's R/V Prof. Besnard (2003/09/28–2003/09/29). As all transects were sampled by CTD vertical profiling only, prior to the selection, we need to compute the geostrophic velocity from the hydrographic data. In order to do so, we decide to employ the method described by Silveira et al. (2004) and simulate the baroclinic velocities numerically by employing a sectional version of the Princeton Ocean Model (POM, e.g., Mellor and Wang, 1996). The observed temperature and salinity fields are used to derive initial conditions. This method does not require an arbitrary choice of reference level, since the baroclinic pressure gradient is numerically computed. Also, it has the advantage of reducing high-frequency noise present in the hydrographic data and adjusting velocity and mass fields to topography.

The numerically-generated velocity section is presented in Fig. 15a. Both BC and IWBC are depicted in the section transporting about 5.8 Sv with their velocity cores aligned vertically. Maximum speeds for the BC (IWBC) are 0.76 m s^{-1} southwestward (0.24 m s^{-1} northeastward). The isotachs in the section depict the BC as a 100 km-wide parabolic current while the IWBC exhibits an elliptical shape and is attached to the continental slope.

The DEPROAS5 velocity profile over the 1200 m isobath (at 23.9°S) compares reasonably well with a 7-month mean calculated from the Marlim current meter mooring (Silveira et al., 2008) (Fig. 15b): correlation coefficient of 0.9, and normalized root mean square error of 0.1 m s^{-1}. Therefore this transect proved to be an appropriate proxy to the mean state of the BC-IWBC system.

Following the transect of choice, we approximate the BC-IWBC current pattern depicted in Fig. 15 by averaging the velocities within the portions of the water column separated by depth of σ_θ. The cross-isobath profiles are shown in Fig. 16a. Moreover, we calculate the purely baroclinic lower profile in a theoretical fashion by multiplying the $\tilde{v}_1$ curve (red in the figure) by $(-\frac{\delta_1}{\delta_2})$. This leads to a null barotropic component, as long as the condition $\bar{x} = \bar{x}_1 = \bar{x}_2$ is satisfied. The comparison between the lower layer average profile (blue curve) and the $-\frac{\delta_1}{\delta_2}\tilde{v}_1$ (cyan curve) is reasonable and the two-layer velocity field derived from data fulfills the basic assumption of the M91 jet vertical shear configuration: No barotropic component.

Table 1
The Control run parameters.

Quantity	Symbol	Value
Deformation radius	R_d	33 km
Upper (lower) layer aspect ratio	δ_1 (δ_2)	0.28 (0.72)
Reduced gravity	g'	9.4 $\times 10^{-3}$
Upper (lower) layer PV jump	Δ_1 (Δ_2)	2.1 (−0.59) $\times 10^{-5}$ s^{-1}
Zeroth (first) mode PV jump	Δ^0 (Δ^1)	0.0 (1.1) $\times 10^{-5}$ s^{-1}
Mean front position	$\bar{x}$	56 km
Upper-layer core velocity	$\bar{v}_1(\bar{x})$	−0.22 m s^{-1}
Lower-layer core velocity	$\bar{v}_2(\bar{x}) = -\frac{\delta_1}{\delta_2}\bar{v}_1(\bar{x})$	0.085 m s^{-1}

We also check the depth inversion on the PV cross-isobath gradient requirement (Charney–Stern–Pedlosky criterion) by computing the two-layer PV frontal structures from the velocity profiles and the σ_θ=26.9 kg m^{-3} topography, i.e.,

$$\tilde{\Pi}_1 = \frac{f + \partial_x \tilde{v}_1}{H_{\sigma_\theta}} \quad \text{and} \quad \tilde{\Pi}_2 = \frac{f + \partial_x \tilde{v}_2}{H - H_{\sigma_\theta}}\,. \tag{14}$$

where Π_i is the ith layer Ertel PV and $H_{\sigma_\theta} = H_{\sigma_\theta}(x)$ represents the varying depth of the referred isopycnal. As its inflections are small compared to the average α_1=500 m and the numerically-generated velocities are in geostrophic balance (see Silveira et al., 2004, for details), we consider

$$\tilde{q}_i = \alpha_i \tilde{\Pi}_i - f \tag{15}$$

as a proxy for the two-layer QG PV cross-isobath profile. The results are shown in Fig. 16b. It is evident that the cross-isobath PV gradient changes sign vertically, therefore, the Charney–Stern–Pedlosky necessary but not sufficient condition for baroclinic instability (Pierrehumbert and Swanson, 1995) is satisfied in our two-layer approximation of the observations. Finally, we determine the modeled core velocity $v_1(\bar{x}_1)$ by requiring the volume transport of the modeled jet to be the same as the one from the two-layer approximation of the DEPROAS5 transect in the upper layer.

Fig. 17 shows the result of the cross-boundary profile of the theoretical jet $\bar{v}_i$ (in red for the BC and blue for the IWBC) and the DEPROAS5 two-layer approximation (in light gray for the BC and dark gray for the IWBC). It is clear that the modeled jet is broader and has gentler lateral shear than the one derived from observations. The core velocity is virtually half of the DEPROAS5 two-layer jet's, which was determined by enforcing the observed 5.8 Sv transport in both BC and IWBC layers. These are the default parameters which will define our Control Run, and are summarized in 1.

4.3. The experiments

We run a set of experiments to explore the dynamics of the system posed and consequently infer the basic dynamics that rule the development of the quasi-stationary meanders under study. We first analyze the linear model and estimate growth rates and phase speeds. We also obtain the modal PV jumps to be used in the nonlinear model simulations 1. In the first set of experiments, we find the linear properties in terms of the front position relative to the western boundary. In the second set of experiments, we keep the front position of the Control Run but add a barotropic component to the velocity fields.

Lastly, we explore the nonlinear model to evaluate the evolution of the PV fronts. Since we are interested in investigating the role of baroclinic instability in our system, the barotropic component is set to be null. We run three experiments: the *Control Run*, in which a single perturbation evolves in the presence of the western boundary;

the *Infinite Jet Run*, in which the same initial condition of the Control Run is set to evolve in an open domain, distant from the boundary; and the *Two-cape Run*, in which we place two perturbations near the boundary to mimic the presence of the two capes, Frio and São Tomé.

4.3.1. Linear model results

We first evaluate the linear model results for the Control Run. In this experiment, wavelengths λ larger than ~220 km are unstable, being the most unstable λ_{max}= 296 km with growth rates $\sigma_{max} \approx 0.056\,day^{-1}$ (Fig. 18a). The absolute phase speeds c are one order of magnitude lower than the upper layer core velocity, hence such waves are quasi-stationary (Fig. 18b).

The linear stability parameters for the Control Run are remarkably similar to the analysis performed by Silveira et al. (2008) using moorings, a continuously-stratified ocean, one-dimensional (in z) QG model, and the BC thermal front position derived from SST images. They found λ_{max} ranging from 250 km to 300 km with $\sigma_{max} \approx 0.06\,day^{-1}$ and the correspondent phase speeds of −0.04 to $0.06\,m\,s^{-1}$. Therefore, the linear model output is encouraging and gives us confidence that our simple idealized setup is capable of reproducing the basic dynamics of the quasi-stationary meanders of the BC-IWBC system.

We then test the linear stability properties of the idealized jet by varying the front position $\bar{x}$ (Fig. 19 left panels). The intent here is to explore and understand the results that yielded the results for the Control Run. We find no significant change in λ_{max} (maximum increase of ~6%), maintaining $\lambda_{max} \simeq 300$ km (Fig. 19a). On the other hand, the $\bar{x}$ strongly influences most unstable waves' (meanders') growth rates σ_{max} (Fig. 19c). That is, the western boundary basically acts as a stabilizing agent for the jet, reducing σ_{max}. However, the western boundary effect on the jet reduces rapidly and has no influence on σ_{max} from an ~80 km front distance. Furthermore, we draw the reader's attention to the fact that the phase speed magnitude c_{max} of the most unstable waves grows exponentially as the front distance from the boundary increases. They reach an asymptotic value of $\sim 0.012\,m\,s^{-1}$ for $\bar{x} > 80$ km, hence virtually null phase speeds (Fig. 19e). Therefore, the front position does not affect the stationarity of the meanders.

Note that the linear model parameters reach an asymptote as $\bar{x}$ increases. More specifically, from a distance of 80 km ($\approx 2.5\,Rd$), the system will present practically the same solutions, i.e., as of an 80 km distance, the system can be seen as evolving far from the western boundary or in an infinite ocean (no lateral boundaries).

We also test the effect of the addition of a barotropic component to the BC-IWBC jet (Fig. 19 right panels). We vary the barotropic core velocity $\bar{v}_{bt}(\bar{x})$ from $-0.22\,m\,s^{-1}$ (southward) to $0.22\,m\,s^{-1}$ (northward). Fig. 20a, b respectively present cross-jet profiles for two illustrative cases within the mentioned parameter space. Unlike the varying $\bar{x}$ experiments, the inclusion of a barotropic component has a more relevant impact on the linear model parameters as they do not reach asymptotic values when evaluated as a function of $\bar{v}_{bt}(\bar{x})$.

The most unstable wavelengths λ_{max} are still kept around 300 km in the chosen parameter space increasing (decreasing) with a southward (northward) barotropic velocity component $\bar{v}_{bt}$ (Fig. 19b). The system becomes relatively more unstable with a northward $\bar{v}_{bt}$ but the most unstable growth rates σ_{max} are not very sensitive to it, increasing ~7% (Fig. 19d) and seem to reach a limit around $0.06\,day^{-1}$. Nevertheless, as for the cases with a southward $\bar{v}_{bt}$, σ_{max} are heavily affected (39% reduction). Such result is probably due to the suppression of baroclinic instability in the presence of a barotropic component to the mean geophysical flow structure (James, 1987). The lateral shear imposed by v_{bt} (note the upper layer velocity inversion in the example shown in Fig. 20a) confines the waves zonally dampening their growth as the shear becomes sharper with a larger southward $\bar{v}_{bt}$.

Lastly, the phase speed of the most unstable wavelength c_{max} is the parameter with the greatest sensitivity to the barotropic component. The perturbations are probably advected downstream of the barotropic jet component almost linearly (Fig. 19f). That is, according to our linear stability analysis, the stationarity of the meanders is due to the first-baroclinic-mode structure of the mean BC-IWBC system almost devoid of a barotropic velocity.

4.3.2. Nonlinear model results

Let us now evaluate the nonlinear evolution of the two-layer system. The CD model restricts the dynamics to the PV front. However, to obtain 2D velocity fields for each layer, we solve the model on a regular Eulerian grid of ~7 km ($0.2\,R_d$) horizontal resolution. We can compute the velocity field by taking the contour position (i.e. the PV front) as the points where the layer velocity is maximum (see red and blue curves in Fig. 17). We then compute the ψ fields by following the Li et al. (2006) method,[4] in which the gridded velocity field is decomposed into non-rotational and non-divergent components through the solution of an

[4] Code available at https://github.com/iuryt/vector_fields.

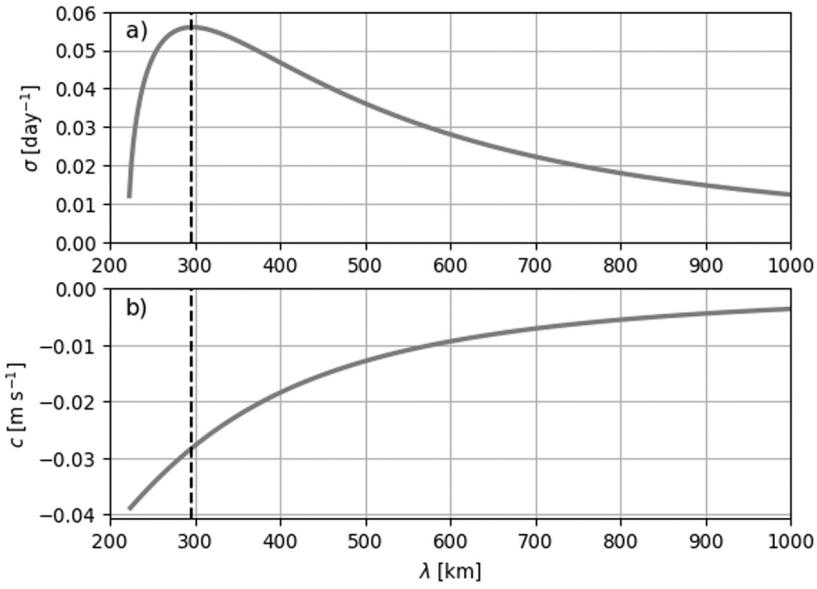

Fig. 18. The linear stability properties for the Control Run setup: (a) growth rates σ and (b) phase speeds c as a function of the wavelength λ. The most unstable wavelength λ_{max} = 296 km is marked by the dashed line.

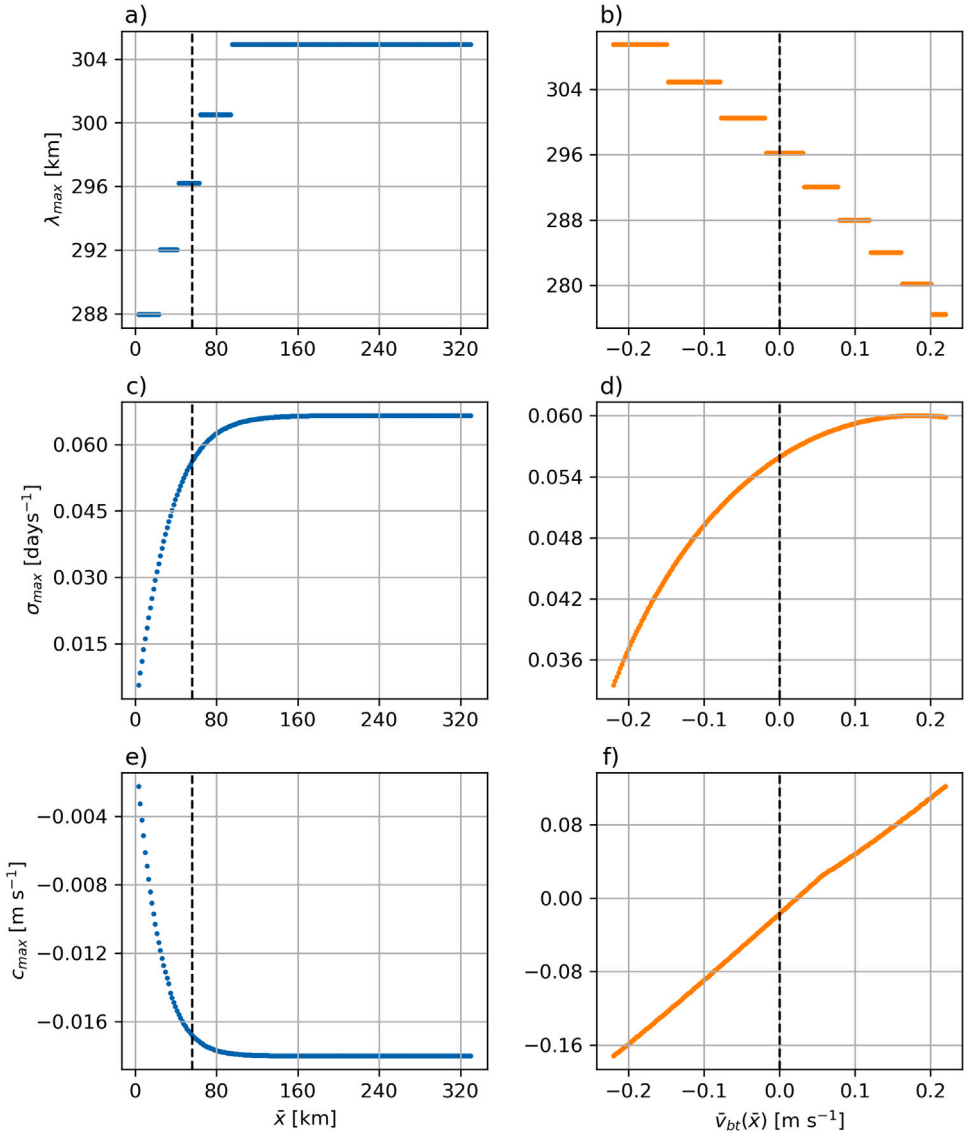

Fig. 19. Wavelength (a, b), growth rate (c, d) and phase speed (e, f) for the most-unstable linear modes as a function of front distance $\bar{x}$ from the western boundary (in blue) and addition of a barotropic velocity $\bar{v}_{bt}$ to the jet (in orange). The dashed vertical lines depict the Control Run values for $\bar{x} = 56$ km and $\bar{v}_{bt} = 0.22$ m s^{-1}.

inverse minimization problem. The gridded ψ fields are not necessary for the CD model but are calculated for visualization purposes.

We mimic the presence of the capes by configuring the Control Run to evolve a single Gaussian perturbation with an amplitude of 70 km, similar dimensions to the path deviation of the mean BC around the capes (Fig. 14). The initial perturbation in the mean front grows quasi-stationary (Fig. 21). Due to the model construction, the meander growth can only occur via baroclinic instability. PV anomalies in one layer interact and enhance the anomalies onto the other (layer coupling). We draw one's attention to Fig. 21a–d concerning this matter. Notice that as soon as the perturbations have slightly moved downstream, the peaks no longer coincide, the flow along both contours moves in the same direction. This baroclinic conversion creates a barotropic component associated with the meander's growth. We also ask the reader to compare Fig. 12 for the OSE4 potential vorticity inversion calculation and Fig. 21d. The CD model seems to capture the same character as that observed in the map derived from *in situ* data.

The 3D perspective of the CD flow brought by the ψ fields in Fig. 21e–l highlights the effect that each layer exerts onto the other; an anticyclonic signal of the lower layer meander emerges in the northern portion of the upper layer eddy (Fig. 21h). The cyclonic signal of the upper layer meander is undeniable in the southern portion of the lower layer meander (Fig. 21i–l), which actually detaches from the main current. We did test the effect of the addition of a barotropic component in the velocity field (not shown). As predicted by the linear model (Fig. 19 right panels), the meander growth is inhibited inasmuch as the barotropic velocity tends to advect the perturbations downstream. This seems to occur because the q_i are altered, due to the inclusion of the barotropic component, increasing in the upper layer, and decreasing in the lower layer.

A rough estimate for λ of the initial condition is ~440 km, which should yield growth rate $\sigma \approx 0.04$ day^{-1} and phase speed of -0.02 m s^{-1}. However, tracking of the red PV contour in Fig. 21 gives an estimated $\sigma \approx 0.02$ day^{-1} in the first 70 days, half of the linear analysis prediction. The nonlinear model is not evolving the most unstable wavelengths either because of nonlinear effects or more probably due to the isolated disturbance pattern. In the latter case, we observed that the presence of the boundary inhibits the development of a wave pattern, which

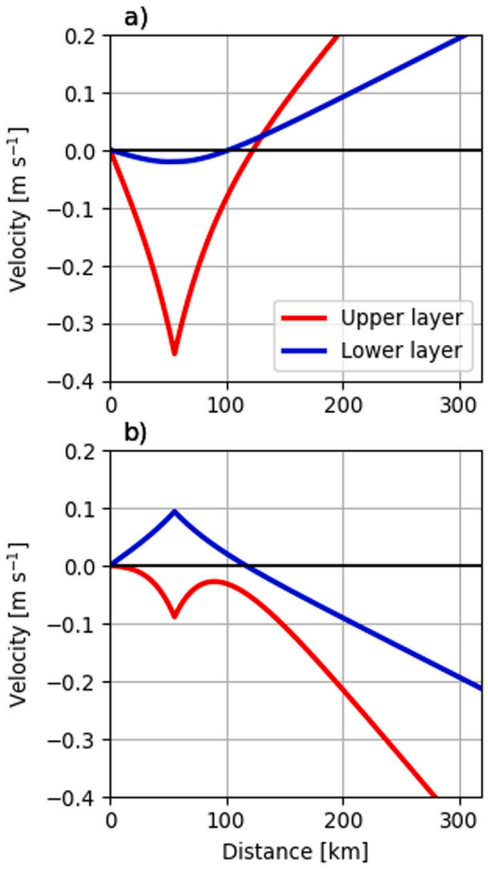

Fig. 20. Cross-jet profiles are also shown for two cases with the addition of a barotropic component core velocity $|\bar{v}_{bt}|(\bar{x}) = 0.07\,\mathrm{m\,s^{-1}}$ (32% of $\bar{v}_1(\bar{x})$) (a) southward, and (b) morthward. $\bar{x}$ =56 km is kept constant. The upper layer jet is depicted in red, and the lower layer one in blue.

tends to be more unstable. Despite the difference in the growth rate, the expected pattern of the flow evolution is present. Such small σ implies that linear growth is a reasonable approximation for the meander growth after the initial days of development.

For the Infinite Jet Run, we take advantage of the linear model predictions (Fig. 19 left panels) and impose $\bar{x}$= 200 km so the jet does not "feel" the western boundary. Fig. 22 shows the evolution of a single perturbation. We observe widespread cyclonic and anticyclonic meander growth in the domain as the perturbations in each layer couple and positively feed growth onto the other. In other words, the presence of the western boundary inhibits the development of anticyclones in the upper layer.

Lastly, we configure an experiment where two initial perturbations, distant ~300 km from one another, are imposed close to the western boundary, the Two-cape Run (Fig. 23). The 300 km distance roughly corresponds to the distance between CF and CST, which is also similar to the most unstable wavelength predicted by the linear stability analysis of the Control Run (Fig. 18a). In this way, we can briefly assess whether meanders growing simultaneously can interact or not (Fig. 2). The western boundary and consequent suppression of anticyclonic growth in the upper layer, isolates each perturbation and they grow independent of each other.

As demonstrated by the Control Run experiments, a highly idealized model is capable of reproducing the basic dynamics, that is, the quasi-stationary growth of the BC-IWBC jet meanders. According to the model outputs, the stationarity of the meanders can indeed be related to the predominant baroclinic nature of the mean BC-IWBC jet, and the western boundary not only slightly stabilizes the jet, but also inhibits the formation of anticyclones in the BC. Furthermore, in scenarios of simultaneous meander growth in both capes, the proximity of the jet to the western boundary also induces the perturbations to baroclinically grow isolated.

5. Summary and final remarks

This study advances knowledge of two of the most conspicuous oceanographic features off Southeast Brazil: the quasi-stationary unstable cyclonic meanders of the Brazil Current (BC) off Cape São Tomé (CSTE) at 22°S and Cape Frio (CFE) at 23°S. These eddies are formed recurrently and can double, sometime triple, the BC velocity as they grow oceanward. In particular, we sought to (1) obtain observational estimates of meander growth rates in the first-baroclinic-mode jet formed by the BC and Intermediate Western Boundary Current (IWBC); (2) search for evidence of baroclinic growth in quasi-synoptic hydrographic cruise observations; and (3) explain why the two-cape region favors the formation of cyclones and why those meanders are quasi-stationary. Our focus is on baroclinic processes and we do not address the possible barotropic growth.

To estimate growth rates and propagation speeds, we used two independent data sets and two different approaches. In a more classical approach based on the BC thermal front, we first analyzed sparse sequences of SST images. The second approach employed continuous series of altimetric maps to estimate growth rates, frequency of stationary growth and propagation (translation) velocity and trajectory direction after they were shed by the BC. By reconciling the SST and SSH analyses, we found that the growth rates were 0.06 day^{-1} on average, phase speeds were about 2%–5% of the typical surface values of the BC. Moreover, we identified about 3.5 (2.3) events per year for the unstable CFE (CSTE). After being shed, only 6% of CSTEs travel northward and 2% migrate southward, while 29% of the CFEs propagate southward.

We next looked for evidence of baroclinic growth in quasi-synoptic data from a Brazilian Navy hydrographic survey (the OSE4 cruise). We used a two-layer approximation for the geostrophic velocity/stream function fields, and computed the quasi-geostrophic potential vorticity. The two-layer model represents the BC and IWBC layers. Our calculations show that the cyclonic anomalies in one layer acted to enhance the anomalies on the other, a strong suggestion of baroclinic instability. We also observed a 45° phase difference between the potential vorticity (PV) lines at the core of the BC and the PV lines at the core of the IWBC, another suggestion that baroclinic conversion was taking place.

Finally, we built a two-layer quasi-geostrophic contour dynamics model for the BC-IWBC system, with parameters inspired by observations. The linear stability properties of this model are remarkably similar to those reported in previous studies and fall in the range of the growth rates and phase speeds in our satellite analyses.

Nonlinear evolution experiments performed with this model led to two main conclusions. First, the quasi-stationarity of the meanders is a consequence of the largely first-mode vertical structure of the BC-IWBC jet. This dynamical structure is also responsible to keep the linear stability properties in the range of the observations. Second, the proximity of the jet to the western boundary has little effect on the most unstable wavelengths but reduces the growth rates and inhibits the formation of anticyclones in the BC domain. Moreover, the western boundary allows perturbations to grow independently on each cape, preventing them from interacting with each other in cases where the meanders may grow simultaneously or not.

Future work should address the triggering mechanisms involved in the generation of these mesoscale disturbances. Also, their spatial scales and quasi-stationarity might have significant implications to the pelagic ecosystem of the region. Investigating those implications as well as cross-shelf exchange of biogeochemical tracers induced by these meanders should be pursued.

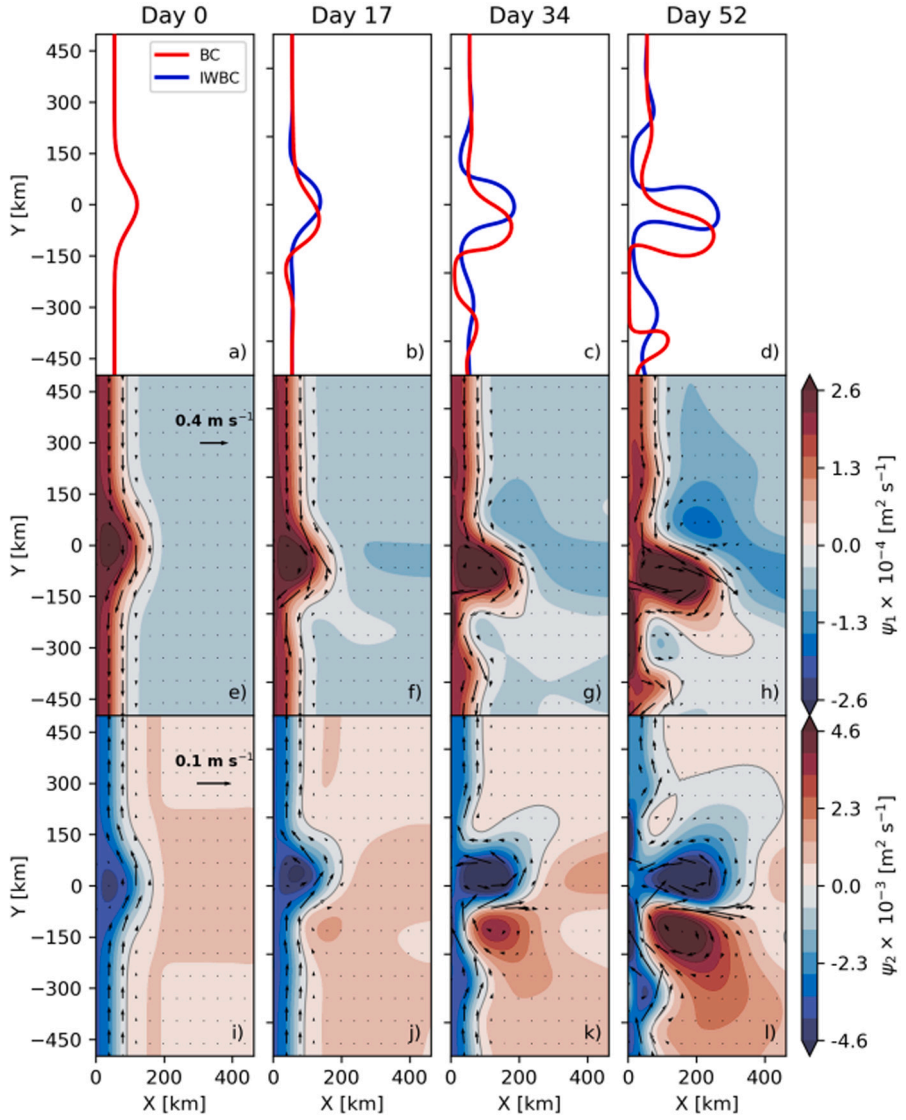

Fig. 21. Control Run: temporal evolution of the potential vorticity fronts or contours (a–d); and horizontal velocity for the upper layer (e–h) and lower layer (i–l).

CRediT authorship contribution statement

Ilson C.A. da Silveira: Conceptualization, Methodology, Software, Formal analysis, Investigation, Data curation, Resources, Writing – original draft, Writing – review & editing, Supervision, Project administration, Funding acquisition. **Filipe Pereira:** Methodology, Software, Formal analysis, Investigation, Data curation, Writing – original draft, Writing – review & editing, Visualization, Supervision. **Glenn R. Flierl:** Conceptualization, Methodology, Software, Formal analysis, Investigation, Writing – review & editing, Supervision. **Iury T. Simoes-Sousa:** Methodology, Software, Formal analysis, Investigation, Writing – original draft, Writing – review & editing, Visualization. **André Palóczy:** Methodology, Formal analysis, Investigation, Writing – review & editing, Visualization. **Milton Borges-Silva:** Software, Writing – review & editing, Visualization. **César B. Rocha:** Conceptualization, Methodology, Investigation, Writing – review & editing, Visualization.

Declaration of competing interest

The authors declare that they have no known competing financial interests or personal relationships that could have appeared to influence the work reported in this paper.

Data availability

OSE4 and DEPROAS5 data sets are made available by the Brazilian Navy upon request via email chm.bndo@marinha.mil.br. More details on how to request the data can be found on https://www.marinha.mil.br/chm/dados-do-bndo/outros-dados-e-produtos.

The Multi-scale Ultra-high Resolution (MUR) Sea Surface Temperature (SST) Analyses is part of the NASA Making Earth System Data Records for Use in Research Environments (MEaSUREs) Program, distributed by the Physical Oceanography Distributed Active Archive Centre (PODAAC) system available at https://podaac.jpl.nasa.gov.

The altimetric Mesoscale Eddy Trajectories Atlas (META3.1exp DT) was produced by SSALTO/DUACS and distributed by AVISO+ (https://aviso.altimetry.fr) with support from CNES, in collaboration with IMEDEA (DOI: 10.24400/527896/a01-2021.001 for the META3.1exp DT allsat version and 10.24400/527896/a01-2021.002 for the META3.1exp DT twosat version).

The Ssalto/Duacs altimeter products were produced and distributed by the Copernicus Marine and Environment Monitoring Service (CMEMS) (https://marine.copernicus.eu/).

General Bathymetric Chart of the Oceans (GEBCO) Compilation Group (2021) GEBCO 2021 Grid (doi:10.5285/c6612cbe-50b3-0cff-e053-6c86abc09f8f) is available at https://www.gebco.net/.

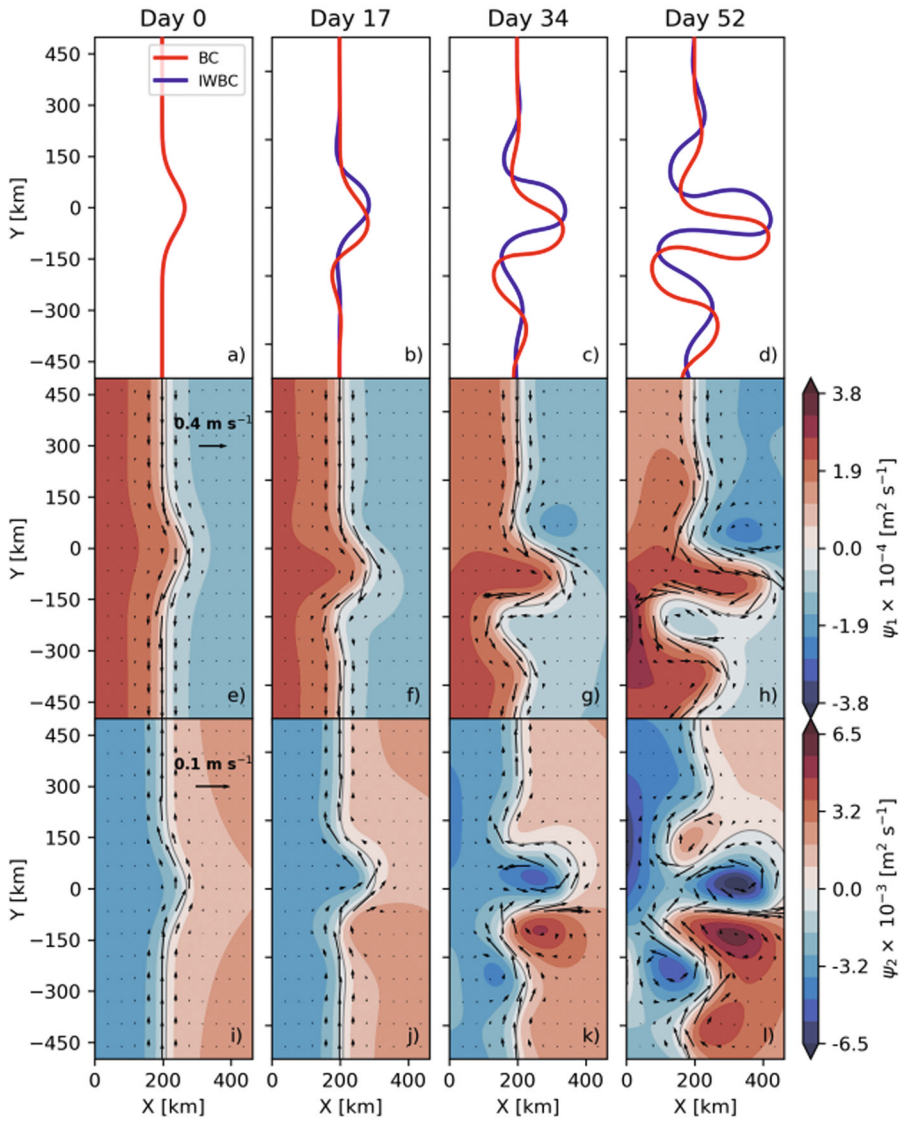

Fig. 22. Infinite Jet Run: temporal evolution of the potential vorticity fronts or contours (a–d); and horizontal velocity for the upper layer (e–h) and lower layer (i–l).

Acknowledgments

I. C. A. da Silveira acknowledges support from the National Council for Scientific and Technological Development (CNPq, Brazil) [309656/2021-4], the São Paulo Research Foundation (FAPESP, Brazil) [2018/23459-2], HIDROSAN Project – CNPq, Brazil [405593/2021-0], and REMARSUL Project – Federal Agency for Support and Evaluation of Higher Education Personnel (CAPES, Brazil) [88882.158621/2014-01]. F. Pereira was supported by FAPESP, Brazil [2017/15026-6]. A. Palóczy acknowledges support from FAPESP, Brazil [2013/11465 4]. C. B. Rocha was supported by the National Science Foundation (NSF, USA) [2146729].The authors thank the efforts of the crew and scientists on the different survey legs of the *R/V Antares* and that of the competent analysts of the *Banco Nacional de Dados Oceanográficos* (BNDO) for making the OSE4 and DEPROAS5 data sets available.

Appendix A. Linear stability properties derived from the sea surface temperature analysis

See Table A.2.

Appendix B. Formulation of the contour dynamics model

The model is governed by the conservation of the quasi-geostrophic potential vorticity in each layer,

$$\frac{D}{Dt} q_i = 0, \tag{B.1}$$

where q_i is given by (2).

Following the formalism presented by Silveira and Flierl (2002), (13) can be split into mean (associated with the jet itself) and perturbed (associated with the meandering) parts:

$$\bar{q}_i = q_{0i} + \Delta_i \mathcal{H}(x - \bar{x}_i)\,, \tag{B.2}$$

and

$$q_i' = \Delta_i [\mathcal{H}(x - \bar{x}_i - \eta_i) - \mathcal{H}(x - \bar{x}_i)]\,, \tag{B.3}$$

respectively. The corresponding inversion relationships are obtained by combining (B.2) and (B.3) with (2) to get

$$\begin{aligned} \nabla^2 \bar{\psi}_1 + \frac{\alpha_1}{R_d^2}(\bar{\psi}_2 - \bar{\psi}_1) &= \bar{q}_1 \\ \nabla^2 \bar{\psi}_2 - \frac{\alpha_2}{R_d^2}(\bar{\psi}_2 - \bar{\psi}_1) &= \bar{q}_2\,. \end{aligned} \tag{B.4}$$

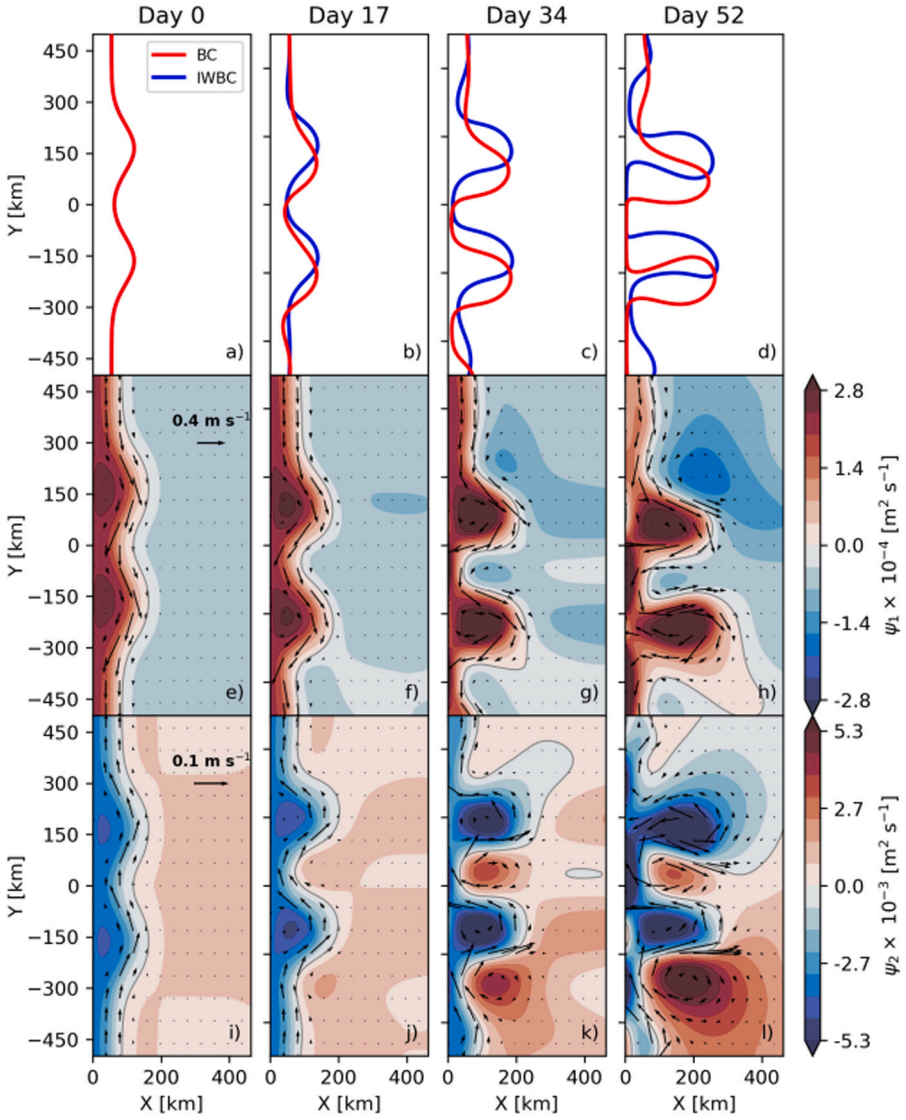

Fig. 23. Two-cape Run: temporal evolution of the potential vorticity fronts or contours (a–d); and horizontal velocity for the upper layer (e–h) and lower layer (i–l).

Table A.2
Quasi-stationary meander properties for selected events estimated from the SST imagery: Growth rate (σ), phase speed (c) and normalized root mean square error (RMSE). Negative phase speeds are in the downstream direction (southward/southwestward).

	Event	σ [day^{-1}]	c [m s^{-1}]	RMSE
Cape Frio (23°S)	2003/06/29 → 2003/07/14	0.102	−0.039	0.109
	2005/05/03 → 2005/05/15	0.121	−0.063	0.072
	2005/06/02 → 2005/06/11	0.079	+0.014	0.113
	2006/07/03 → 2006/07/23	0.062	−0.038	0.073
	2009/06/16 → 2009/06/26	0.131	−0.095	0.053
	2010/04/12 → 2010/04/23	0.120	−0.097	0.052
	2013/04/29 → 2013/05/07	0.254	−0.137	0.151
	2014/10/21 → 2014/10/30	0.080	−0.072	0.053
	2017/05/31 → 2017/06/17	0.082	−0.026	0.044
	2018/04/24 → 2018/05/08	0.069	−0.037	0.039
	2019/09/26 → 2019/10/07	0.087	−0.103	0.063
	2020/08/29 → 2020/09/12	0.113	−0.089	0.047
Cape São Tomé (22°S)	2002/10/27 → 2002/11/08	0.080	+0.054	0.054
	2006/01/24 → 2006/02/08	0.094	−0.057	0.086
	2011/03/13 → 2011/03/23	0.181	−0.166	0.073
	2013/02/22 → 2013/03/11	0.154	−0.049	0.139
	2013/12/24 → 2014/01/02	0.077	−0.062	0.107
	2015/01/01 → 2015/01/18	0.071	+0.028	0.034
	2015/12/22 → 2016/01/03	0.129	−0.079	0.073
	2018/02/05 → 2018/02/17	0.094	−0.105	0.100
	2020/12/31 → 2021/01/11	0.188	−0.074	0.097

and

$$\nabla^2\psi_1' + \frac{\alpha_1}{R_d^2}(\psi_2' - \psi_1') = q_1'$$
$$\nabla^2\psi_2' - \frac{\alpha_2}{R_d^2}(\psi_2' - \psi_1') = q_2' \,. \tag{B.5}$$

Considering $v_i = \partial\psi_i/\partial x$, we can also derive (B.5) with respect to x to obtain the inversion relationship for the Meacham (1991) mean jet:

$$\nabla^2\bar{v}_1 + \frac{\alpha_1}{R_d^2}(\bar{v}_2 - \bar{v}_1) = \Delta_1\,\delta(x - \bar{x}_1)$$
$$\nabla^2\bar{v}_2 - \frac{\alpha_2}{R_d^2}(\bar{v}_2 - \bar{v}_1) = \Delta_2\,\delta(x - \bar{x}_2)\,. \tag{B.6}$$

where $\delta(x)$ is the Dirac delta function.

We also rewrite (B.1), given the PV front is a material line, in terms of the kinematic relationships:

$$\frac{D\eta_i}{Dt} = u_i'\,; \quad \frac{Dy_i}{Dt} = \bar{v}_i + v_i'\,. \tag{B.7}$$

B.1. The linear model

Eqs. (B.5), (B.6), and (B.7) can be linearized about $\bar{x}_i$ and solved by considering solutions of the form

$$\begin{pmatrix}\eta_i\\ \psi_i'\\ u_i'\\ v_i'\end{pmatrix} = \begin{pmatrix}\hat{\eta}_i\\ \hat{\psi}_i\\ \hat{u}_i\\ \hat{v}_i\end{pmatrix} e^{il(y-ct)}\,, \tag{B.8}$$

where l is the meridional wavenumber and $c = \omega/l$ is the complex meridional phase speed. The linearized equations then become:

$$\left(\frac{\partial^2}{\partial x^2} - l^2\right)\hat{\psi}_1 + \frac{\alpha_2}{R_d^2}(\hat{\psi}_2 - \hat{\psi}_1) = -\Delta_1\,\hat{\eta}_1\,\delta(x - \bar{x}_1)$$
$$\left(\frac{\partial^2}{\partial x^2} - l^2\right)\hat{\psi}_2 - \frac{\alpha_1}{R_d^2}(\hat{\psi}_2 - \hat{\psi}_1) = -\Delta_2\,\hat{\eta}_2\,\delta(x - \bar{x}_2) \tag{B.9}$$

for the PV inversion relative to the stream function anomalies;

$$\frac{\partial^2\bar{v}_1}{\partial x^2} + \frac{\alpha_1}{R_d^2}(\bar{v}_2 - \bar{v}_1) = \Delta_1\,\delta(x - \bar{x}_1)$$
$$\frac{\partial^2\bar{v}_2}{\partial x^2} - \frac{\alpha_2}{R_d^2}(\bar{v}_2 - \bar{v}_1) = \Delta_2\,\delta(x - \bar{x}_2) \tag{B.10}$$

for the mean meridional jet inversion relationship; and

$$\bar{v}_1(\bar{x}_1)\,\hat{\eta}_1 - c\,\hat{\eta}_1 = \hat{\psi}_1(\bar{x}_1)$$
$$\bar{v}_2(\bar{x}_2)\,\hat{\eta}_2 - c\,\hat{\eta}_2 = \hat{\psi}_2(\bar{x}_2)\,, \tag{B.11}$$

are the linearized Lagrangian equations.

Both sets of (B.9) and (B.10) can be solved by using Green's functions. Our linear model solution differs from that presented by Meacham (1991) by imposing the presence of a western boundary at $x = 0$. For the present case, the Green's function associated with the mth mode on the ith layer due to PV sources on the jth layer is given by;

$$G_{ij}(x|x') = \sum_m \alpha_i\,F_i^m\,F_j^m\,G^{(m)}\,, \tag{B.12}$$

where

$$G^{(0)}(x|x') = -\frac{1}{2}\left(|x - x'| - |x + x'|\right) \tag{B.13}$$

for the barotropic mode ($m = 0$), and

$$G^{(1)}(x|x') = -\frac{1}{2\sqrt{l^2 + R_d^{-2}}}\left[e^{\left(\sqrt{l^2+R_d^{-2}}\,|x-x'|\right)} - e^{\left(\sqrt{l^2+R_d^{-2}}\,|x+x'|\right)}\right] \tag{B.14}$$

for the baroclinic mode ($m = 1$). The combination of (B.9) and (B.10) with (B.14) and (B.13) yields

$$\hat{\psi}_i = \sum_j G_{ij}(x - x')\,\Delta_j\,\hat{\eta}_j\,, \tag{B.15}$$

and

$$\bar{v}_i = \sum_j G_{ij}(x - x')\,\Delta_j\,. \tag{B.16}$$

We can thus solve for c using (B.11) by evaluating $(\psi_i', \bar{v}_i)$ at $\bar{x}_i$. Additionally, it is more convenient to specify the basic jet velocities at the contours rather than at the Δ_i. The layer PV jumps are found by inverting (B.16) (Silveira and Flierl, 2002). Also, we can compute the modal PV jumps by applying the same relationship expressed in (5) to the layer PV jump values.

Lastly, unlike in the Meacham (1991) original jet model, where the ith-layer inshore PV q_{0_i} value is a free and arbitrarily chosen parameter, in the presence of the western boundary, its value is set by the $\bar{\psi}_i(0) = 0$ boundary condition yielding

$$q_{0i} = -\frac{1}{R_d}\left[\frac{\alpha_i\,F_i^1\,\Delta_i}{\sinh\left(\bar{x}/R_d\right) + \cosh\left(\bar{x}/R_d\right)}\right]. \tag{B.17}$$

B.2. The nonlinear model

The full nonlinear system is also solved using Green's functions. The solution of (B.5) becomes

$$\psi_i(x, y, t) = \sum_j \frac{\Delta_j}{2\pi}\iint_{A_j} G_{ij}(x, y|x', y')dx'\,dy', \tag{B.18}$$

where A_j is the area between the curves $\bar{x}_j + \eta_j$ and $\bar{x}_j$. The elements of the Green's function matrix which satisfy the $\psi'(0, y, t) = u'(0, y, t) = v'(0, y, t) = 0$ boundary condition are given by

$$G_{ij}(r) = -\sum_m \alpha_i F_i^m F_j^m G^{(m)}\,, \tag{B.19}$$

where the Green's function for the barotropic ($G^{(0)}(r)$) and baroclinic mode ($G^{(1)}(r)$) equations are

$$G^{(0)}(r) = \ln(r_+) - \ln(r_-) \tag{B.20}$$
$$G^{(1)}(r) = K_0\left(\frac{r_+}{R_d}\right) - K_0\left(\frac{r_-}{R_d}\right), \tag{B.21}$$

respectively. $K_0(\frac{r}{R_d})$ is the modified Bessel function of the second kind and zeroth order, and r_+ and r_- are defined as

$$r_+ = \sqrt{(x - x')^2 + (y - y')^2}\,, \tag{B.22}$$
$$r_- = \sqrt{(x + x')^2 + (y - y')^2}\,. \tag{B.23}$$

The expressions for the anomaly velocities are obtained by differentiating (B.18) using the symmetry properties of the Green's function and applying the divergence theorem (see Silveira et al., 1999 for details). In doing so, we obtain

$$u_i' = \sum_j \frac{\Delta_j}{2\pi}\int_{\partial A_j} G_{ij}(r)\,dx'\,, \tag{B.24}$$

and

$$v_i' = \sum_j \frac{\Delta_j}{2\pi}\int_{\partial A_j} G_{ij}(r)\,dy'\,. \tag{B.25}$$

where ∂A_j is the contour enclosing the area A_j.

The contour algorithm employed in this work closely follows that described by Silveira and Flierl (2002). The algorithm tracks the contour (i.e., the PV front) as a set of Lagrangian points with the positions advancing according to the kinematic equations. A second-order Runge–Kutta scheme is used in the discretization of (B.7) together with the basic jet velocity $\bar{v}$ calculated from (B.16) and the perturbed velocities u' and v' evaluated from (B.24) and (B.25). The latter expressions are discretized using a midpoint integration rule. In order to maintain the model's resolution, we apply a simple particle insertion-deletion scheme to keep the particle separation within a predefined range.

References

Arruda, W.Z., Campos, E.J., Zharkov, V., Soutelino, R.G., Silveira, I.C.A.d., 2013. Events of equatorward translation of the Vitoria Eddy. Cont. Shelf Res. 70, 61–73. http://dx.doi.org/10.1016/j.csr.2013.05.004.

Arruda, W.Z., Silveira, I.C.A.d., 2019. Dipole-induced central water extrusions south of Abrolhos Bank (Brazil, 20.5°S). Cont. Shelf Res. 188, 103976. http://dx.doi.org/10.1016/j.csr.2019.103976.

Ballarotta, M., Ubelmann, C., Pujol, M.-I., Taburet, G., Fournier, F., Legeais, J.-F., Faugère, Y., Delepoulle, A., Chelton, D., Dibarboure, G., et al., 2019. On the resolutions of ocean altimetry maps. Ocean Sci. 15 (4), 1091–1109. http://dx.doi.org/10.5194/os-15-1091-2019.

Biló, T.C., Silveira, I.C.A.d., Belo, W.C., Castro, B.M., Piola, A.R., 2014. Methods for estimating the velocities of the Brazil Current in the pre-salt reservoir area off southeast Brazil (23°–26°S). Ocean Dyn. 64 (10), 1431–1446. http://dx.doi.org/10.1007/s10236-014-0761-2.

Böebel, O., Davis, R.E., Ollitrault, M., Peterson, R.G., Richard, P.L., Schmid, C., Zenk, W., 1999. The intermediate depth circulation of the Western South Atlantic. Geophys. Res. Lett. 26 (21), 3329–3332. http://dx.doi.org/10.1029/1999GL002355.

Bretherton, F.P., Davis, R.E., Fandry, C., 1976. A technique for objective analysis and design of oceanographic experiments applied to MODE-73. Deep Sea Res. Oceanogr. Abstracts 23 (7), 559–582. http://dx.doi.org/10.1016/0011-7471(76)90001-2.

Calado, L., Gangopadhyay, A., Silveira, I.C.A.d., 2008. Feature–oriented regional modeling and simulations (FORMS) for the western South Atlantic: Southeastern Brazil region. Ocean Model. 25 (1), 48–64. http://dx.doi.org/10.1016/j.ocemod.2008.06.007.

Chin, T.M., Milliff, R.F., Large, W.G., 1998. Basin-scale, high-wavenumber sea surface wind fields from a multiresolution analysis of scatterometer data. J. Atmos. Ocean. Technol. 15 (3), 741–763. http://dx.doi.org/10.1175/1520-0426(1998)015<0741:BSHWSS>2.0.CO;2.

Chin, T.M., Vazquez-Cuervo, J., Armstrong, E.M., 2017. A multi-scale high-resolution analysis of global sea surface temperature. Remote Sens. Environ. 200, 154–169. http://dx.doi.org/10.1016/j.rse.2017.07.029.

Costa, V.S., Mill, G.N., Gabioux, M., Grossmann-Matheson, G.S., Paiva, A.M., 2017. The recirculation of the Intermediate Western Boundary Current at the Tubarão Bight – Brazil. Deep Sea Res. I 120, 48–60. http://dx.doi.org/10.1016/j.dsr.2016.12.001.

Fernandes, A.M., Silveira, I.C.A.d., Calado, L., Campos, E.J.D., Paiva, A.M., 2009. A two-layer approximation to the Brazil Current–Intermediate Western Boundary Current System between 20°S and 28°S. Ocean Model. 29 (2), 154–158. http://dx.doi.org/10.1016/j.ocemod.2009.03.008.

Firing, E., Hummon, J.M., 2010. Shipboard ADCP Measurements. In: Hood, E., Sabine, C., Sloyan, B. (Eds.), The GO-SHIP Repeat Hydrography Manual: A Collection of Expert Reports and Guidelines. http://dx.doi.org/10.25607/OBP-1352, IOCCP Report Number 14, ICPO Publication Series Number 134. Available Online At: http://www.go-ship.org/hydroman.html.

Flierl, G.R., 1978. Models of vertical structure and the calibration of two-layer models. Dyn. Atmos. Oceans 2 (4), 341–381. http://dx.doi.org/10.1016/0377-0265(78)90002-7.

Garfield, N., 1990. The Brazil current at subtropical latitudes (Ph.D. thesis). University of Rhode Island, Kingston, United States, 122 pp..

Guerra, L.A.A., Paiva, A.M., Chassignet, E.P., 2018. On the translation of Agulhas rings to the western South Atlantic Ocean. Deep Sea Res. I Oceanogr. Res. Pap. (ISSN: 0967-0637) 139, 104–113. http://dx.doi.org/10.1016/j.dsr.2018.08.005.

James, I.N., 1987. Suppression of baroclinic instability in horizontally sheared flows. J. Atmos. Sci. 44 (24), 3710–3720. http://dx.doi.org/10.1175/1520-0469(1987)044<3710:SOBIIH>2.0.CO;2.

Legeais, J.-F., Ollitrault, M., Arhan, M., 2013. Lagrangian observations in the Intermediate Western Boundary Current of the South Atlantic. Deep Sea Res. II Topical Stud. Oceanogr. 85, 109–126. http://dx.doi.org/10.1016/j.dsr2.2012.07.028.

Li, Z., Chao, Y., McWilliams, J.C., 2006. Computation of the streamfunction and velocity potential for limited and irregular domains. Mon. Weather Rev. 134 (11), 3384–3394. http://dx.doi.org/10.1175/MWR3249.1.

Lorenzzetti, J., Stech, J., Mello Filho, W., Assireu, A., 2009. Satellite observation of Brazil Current inshore thermal front in the SW South Atlantic: Space/time variability and sea surface temperatures. Cont. Shelf Res. 29 (17), 2061–2068. http://dx.doi.org/10.1016/j.csr.2009.07.011.

Mano, M.F., Paiva, A.M., Torres Jr., A.R., Coutinho, A.L., 2009. Energy flux to a cyclonic eddy off Cabo Frio, Brazil. J. Phys. Oceanogr. 39 (11), 2999–3010. http://dx.doi.org/10.1175/2009JPO4026.1.

Mascarenhas Jr., A.S., Miranda, L.B., Rock, N.J., 1971. A study of the oceanographic conditions in the region of Cabo Frio. In: Costlow Jr., J.D. (Ed.), Fertility of the Sea, vol. 1. Gordon and Breach, pp. 285–308.

Mason, E., Pascual, A., McWilliams, J.C., 2014. A new sea surface height–based code for oceanic mesoscale eddy tracking. J. Atmos. Ocean. Technol. 31 (5), 1181–1188. http://dx.doi.org/10.1175/JTECH-D-14-00019.1.

Meacham, S.P., 1991. Meander evolution on piecewise-uniform, quasi-geostrophic jets. J. Phys. Oceanogr. 21 (8), 1139–1170. http://dx.doi.org/10.1175/1520-0485(1991)021<1139:MEOPUQ>2.0.CO;2.

Mellor, G.L., Wang, X.H., 1996. Pressure compensation and the bottom boundary layer. J. Phys. Oceanogr. 26 (10), 2214–2222. http://dx.doi.org/10.1175/1520-0485(1996)026<2214:PCATBB>2.0.CO;2.

Mémery, L., Arhan, M., Álvarez-Salgado, X.A., Messias, M.-J., Mercier, H., Castro, C.G., Rios, A.F., 2000. The water masses along the western boundary of the south and equatorial Atlantic. Prog. Oceanogr. 47 (1), 69–98. http://dx.doi.org/10.1016/S0079-6611(00)00032-X.

Mill, G.N., da Costa, V.S., Lima, N.D., Gabioux, M., Guerra, L.A.A., Paiva, A.M., 2015. Northward migration of Cape São Tomé rings, Brazil. Cont. Shelf Res. 106, 27–37. http://dx.doi.org/10.1016/j.csr.2015.06.010.

Napolitano, D.C., Silveira, I.C.A.d., Rocha, C.B., Flierl, G.R., Calil, P.H., Martins, R.P., 2019. On the steadiness and instability of the Intermediate Western Boundary Current between 24°and 18°S. J. Phys. Oceanogr. 49 (12), 3127–3143. http://dx.doi.org/10.1175/JPO-D-19-0011.1.

Othman, Z., Abdullah, A., Prabuwono, A.S., 2012. A statistical approach of multiple resolution levels for canny edge detection. In: Proceedings of the 12th International Conference on Intelligent Systems Design and Applications. ISDA, IEEE Organized by Institute of Electrical and Electronic Engineers (IEEE), Kochi, India, pp. 837–841. http://dx.doi.org/10.1109/ISDA.2012.6416646.

Pegliasco, C., Delepoulle, A., Morrow, R., Faugère, Y., Dibarboure, G., 2021. META3.1exp : A new global mesoscale eddy trajectories atlas derived from altimetry. Earth Syst. Sci. Data Discuss. 2021, 1–31. http://dx.doi.org/10.5194/essd-2021-300.

Pierrehumbert, R.T., Swanson, K.L., 1995. Baroclinic instability. Annu. Rev. Fluid Mech. 27 (1), 419–467. http://dx.doi.org/10.1146/annurev.fl.27.010195.002223.

Ramanantsoa, J.D., Krug, M., Penven, P., Rouault, M., Gula, J., 2018. Coastal upwelling south of Madagascar: Temporal and spatial variability. J. Mar. Syst. 178, 29–37. http://dx.doi.org/10.1016/j.jmarsys.2017.10.005.

Rocha, C.B., Silveira, I.C.A.d., Castro, B.M., Lima, J.A.M., 2014. Vertical structure, energetics, and dynamics of the Brazil Current System at 22°S – 28°S. J. Geophys. Res.: Oceans 119 (1), 52–69. http://dx.doi.org/10.1002/2013JC009143.

Schmid, C., Majumder, S., 2018. Transport variability of the Brazil Current from observations and a data assimilation model. Ocean Sci. 14 (3), 417–436. http://dx.doi.org/10.5194/os-14-417-2018.

Silveira, I.C.A.d., Brown, W.S., Flierl, G.R., 2000. Dynamics of the North Brazil Current retroflection region from the Western Tropical Atlantic Experiment observations. J. Geophys. Res.: Oceans 105 (C12), 28559–28583. http://dx.doi.org/10.1029/2000JC900129.

Silveira, I.C.A.d., Calado, L., Castro, B.M., Cirano, M., Lima, J.A.M., Mascarenhas, A.S., 2004. On the baroclinic structure of the Brazil Current-Intermediate Western Boundary Current System. Geophys. Res. Lett. 31 (14), L14308. http://dx.doi.org/10.1029/2004GL020036.

Silveira, I.C.A.d., Flierl, G.R., 2002. Eddy formation in 2-$\frac{1}{2}$ layer, quasigeostrophic jets. J. Phys. Oceanogr. 32 (3), 729–745. http://dx.doi.org/10.1175/1520-0485(2002)032<0729:EFILQJ>2.0.CO;2.

Silveira, I.C.A.d., Flierl, G.R., Brown, W.S., 1999. Dynamics of separating western boundary currents. J. Phys. Oceanogr. 29 (2), 119–144. http://dx.doi.org/10.1175/1520-0485(1999)029<0119:DOSWBC>2.0.CO;2.

Silveira, I.C.A.d., Lima, J.A.M., Schmidt, A.C.K., Ceccopieri, W., Sartori, A., Francisco, C.P.F., Fontes, R.F.C., 2008. Is the meander growth in the Brazil Current system off Southeast Brazil due to baroclinic instability? Dyn. Atmos. Oceans 45 (3), 187–207. http://dx.doi.org/10.1016/j.dynatmoce.2008.01.002.

Silveira, I.C.A.d., Schmidt, A.C.K., Campos, E.J.D., Godoi, S.S., Ikeda, Y., 2000b. A Corrente do Brasil ao largo da costa leste brasileira. Rev. Brasileira Oceanografia 48 (2), 171–183. http://dx.doi.org/10.1590/S1413-77392000000200008.

Souza, L.S.d., Sgarbi, G.N.C., 2019. Bacia de Santos no Brasil: geologia, exploração e produção de petróleo e gás natural. Boletín Geol 41 (1), 175–195. http://dx.doi.org/10.18273/revbol.v41n1-2019009.

Stramma, L., England, M., 1999. On the water masses and mean circulation of the South Atlantic Ocean. J. Geophys. Res. 104 (C9), 20863–20883. http://dx.doi.org/10.1029/1999JC900139.

Taburet, G., Sanchez-Roman, A., Ballarotta, M., Pujol, M.-I., Legeais, J.-F., Fournier, F., Faugere, Y., Dibarboure, G., 2019. DUACS DT2018: 25 years of reprocessed sea level altimetry products. Ocean Sci. 15 (5), 1207–1224. http://dx.doi.org/10.5194/os-15-1207-2019.

Talley, L.D., Pickard, G.L., Emery, W.J., Swift, J.H., 2011. Descriptive Physical Oceanography: An Introduction, 6 Academic Press, ISBN: 978-0-7506-4552-2, http://dx.doi.org/10.1016/C2009-0-24322-4.

Vazquez-Cuervo, J., Dewitte, B., Chin, T.M., Armstrong, E.M., Purca, S., Alburqueque, E., 2013. An analysis of SST gradients off the Peruvian Coast: The impact of going to higher resolution. Remote Sens. Environ. 131, 76–84. http://dx.doi.org/10.1016/j.rse.2012.12.010.

Zabusky, N.J., Hughes, M.H., Roberts, K.V., 1979. Contour dynamics for the Euler equations in two dimensions. J. Comput. Phys. 30 (1), 96–106. http://dx.doi.org/10.1016/0021-9991(79)90089-5.